Journal of Materials Chemistry A

Recent Advances in Characterization of Rechargeable Battery Materials via Scanning Probe Microscopy

Journal:	*Journal of Materials Chemistry A*
Manuscript ID	TA-PER-08-2024-005975.R2
Article Type:	Perspective
Date Submitted by the Author:	27-Dec-2024
Complete List of Authors:	Russell, Joshua; Boise State University Davis, Paul; Boise State University, Micron School of Materials Science & Engineering Efaw, Corey M.; Boise State University Xiong, Hui; Boise State University, Materials Science and Engineering

Title: Recent Advances in Characterization of Rechargeable Battery Materials via Scanning Probe Microscopy

Joshua A. Russell,[1] Paul H. Davis, [1] Corey M. Efaw, [1] Hui Xiong[1,*]

[1]Micron School of Materials Science and Engineering, Boise State University, Boise, ID, 83725, USA

*Corresponding author: Hui Xiong: clairexiong@boisestate.edu

Abstract: Numerous challenges exist in fully understanding current lithium-ion battery (LIB) technology and commercializing "beyond LIBs" that could help support reaching net-zero carbon emissions in the future. These highly complex systems undergo many dynamic processes at different time and length scales, including ion conduction, interphase formation, and degradation, that can be challenging to capture with traditional characterization tools. As a result, scanning probe microscopy (SPM) has become an invaluable platform for enhancing the understanding of these complex and important processes. SPM can be used to obtain topographical, mechanical, electrical, and electrochemical information on a wide range of materials in a variety of environments, including *in situ* and *operando* studies. In this perspective, we briefly describe the operating principles of LIBs and a number of relevant SPM techniques, followed by presenting recent highlights of SPM's unique capabilities as a characterization tool for battery systems. Finally, we offer recommendations for the improvement of SPM studies of battery materials as well as future outlooks.

1. INTRODUCTION

Lithium-ion batteries (LIBs) have become ubiquitous since they were first commercialized in 1991, dominating the portable electronics market and finding applications in grid-scale energy storage and electric transportation systems due to their high energy density, high power density, and long cycle life.[1,2] However, numerous challenges exist in both the understanding of current LIB technology and the implementation of "beyond Li-ion batteries," such as all-solid-state batteries and Na-ion batteries. This is in part due to the high degree of complexity within a battery system; processes within the battery such as interphase formation, ion intercalation, mass transport, and charge transfer occur at a collection of interfaces over a range of length and time scales. For example, ion (de)intercalation in and out of a layered electrode material can cause phase transformations, volume contraction/expansion, and stress-induced cracking at the internal interfaces between the active material and its surrounding conductive matrix, hampering future battery operation. Each of these processes is governed by a correlated set of mechanical, chemical, morphological, and electrical properties that must be considered in order to fully understand the operation and failure of battery systems.

Traditional characterization methods such as scanning electron microscopy (SEM) and transmission electron microscopy (TEM) are often used to observe the morphology, structure, and composition of materials. Electrical information is frequently characterized by two- or four-point conductivity measurements and electrochemical impedance spectroscopy (EIS), while crystal structure is characterized by X-ray diffraction (XRD) and mechanical properties by various indentation methods and tensile tests. However, these characterization techniques possess limitations. Some, such as XRD, only provide information regarding the global/average properties of the material. Among methods that can resolve local properties, such as TEM, complex sample preparation may be required, potentially altering the native chemistry and morphology of the material. In addition, the exposure to high vacuum and large electron fluxes experienced during electron microscopy can damage fragile battery materials, especially during postmortem characterization of cycled samples.

In contrast, scanning probe microscopy (SPM) methods are well-suited to local nanoscale surface characterization of battery materials. SPM methods allow quantitative nanoscale characterization of nearly any solid surface in a wide array of environments (e.g., vacuum, ambient, or fluid) on scales ranging from Ångströms to tens of microns. In SPM, piezoelectric elements are used to precisely raster scan the eponymous probe over the sample surface as tip-sample interaction measurements are conducted at discrete points to generate a 2D array of data that can be converted into a 3D or 4D image[3]. Scanning tunneling microscopy (STM), which uses the quantum mechanical tunneling current between a conductive sample and metallic probe to maintain a constant Å-level tip-sample separation while scanning the surface topography, was the first SPM technique to be reported[4]. Since then, a number of SPM techniques or modes with fewer restrictions on the sample and tip capable of measuring the surface topography and more have been developed. Accordingly, a single modern SPM platform can enable simultaneous measurements of morphology, mechanical, and electrical or magnetic properties. These measurements can yield information about the nanoscale morphological and property heterogeneity that governs the operation and failure of a rechargeable battery, which would be challenging to obtain or fully inaccessible by other techniques. More specialized methods can be used to probe electrochemical reactions, nanoscale chemical composition, and even the structure of liquid electrolytes.

In this perspective, the working principles of rechargeable batteries will first be briefly explained, and a number of the most common SPM techniques applied to LIBs and beyond will be presented. Then, we summarize recent works within the past few years focused on the application of SPM to specific topics within battery systems (e.g., the electrode-electrolyte interface, cathode material degradation, solid electrolytes). Finally, we provide recommendations and an outlook on the status and

future of SPM characterization of battery materials.

2. OVERVIEW OF RECHARGEABLE BATTERIES

2.1 Working Principles of Lithium-Ion Batteries

LIBs operate by a "rocking-chair" mechanism; that is, during discharge Li ions move within the ion-conducting and electron-impeding electrolyte from anode to cathode, while electrons travel externally along the same direction providing electricity, and vice versa (Fig. 1)[5]. It should be noted that both electrodes undergo reduction and oxidation during charge-discharge cycles and therefore both serve as a cathode when reduction occurs or an anode when oxidation takes place; for consistency, we use "cathode" and "anode" throughout this perspective to refer to the positive (higher electrode potential) and negative (lower electrode potential) electrodes, respectively)[6].

Because electrolytes are in contact with all other components of the battery, they have perhaps the highest number of demands placed on them of any component[7]. They must maximize their ionic conductivity, dielectric constant, and compatibility with the electrodes in use, while minimizing viscosity, flammability, and side reactions[6]. Typical electrolytes for LIBs consist of a mixture of one or more nonaqueous solvents, most often carbonates, with a lithium salt solute such as lithium hexafluorophosphate ($LiPF_6$) or lithium perchlorate ($LiClO_4$). In almost all modern LIBs, the chemical potential of one or both electrodes will at some point exceed the thermodynamic stability window of the electrolyte (Fig. 2). When the chemical potential of the anode exceeds the energy of the lowest unoccupied molecular orbital (LUMO) of the electrolyte, electrons will flow to the electrolyte, reducing it. The inverse is true at the cathode when its chemical potential is at lower energy than the highest occupied molecular orbital (HOMO) of the electrolyte; in this case, the electrolyte will be oxidized. This leads to the formation of a solid-electrolyte interphase (SEI) or cathode-electrolyte interphase (CEI), respectively[8]. SEI and CEI are mixed organic-inorganic films of electrolyte decomposition products on the surface of an electrode. These interphase layers are so termed because of their electrolyte-like characteristics; ideally, they should block the movement of electrons to prevent further charge consumption but allow the movement of ions. There is some capacity loss associated with interphase formation, usually confined to the first few cycles, but this "necessary evil" allows the passivation of the electrodes from further

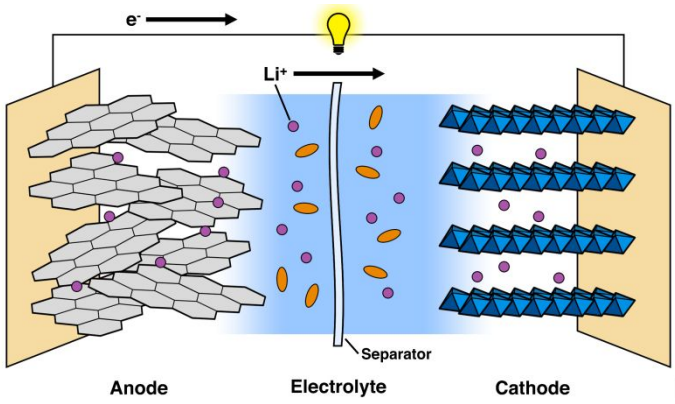

Figure 1. Scheme of a modern lithium-ion battery during discharge.

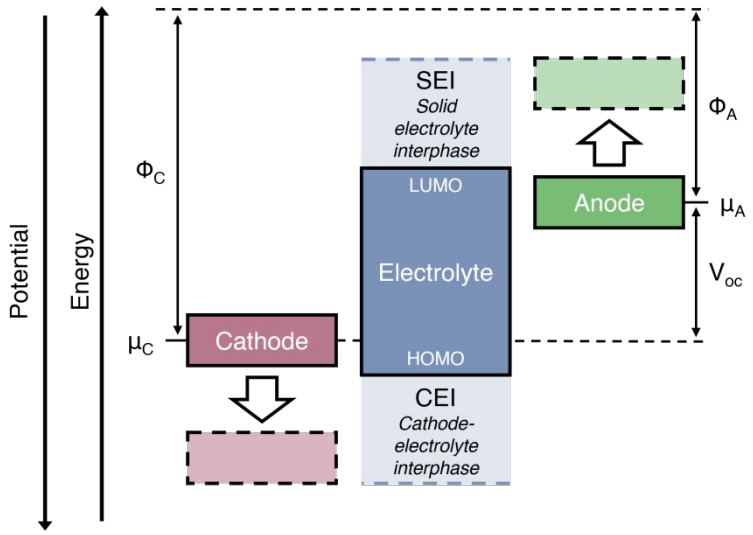

Figure 2. Scheme showing the energetics of SEI and CEI formation in an electrochemical system. ϕ_A and ϕ_C are the work functions of the anode and cathode, μ_A and μ_C are the potentials of the anode and cathode, and V_{oc} is the open circuit potential. Adapted with permission from ref[8]. Copyright 2010 American Chemical Society.

reactions with the electrolyte[6,9]. Despite its importance to the operation of modern LIBs, these interphases remain "the least understood"[10] due to the difficulty of characterizing the thin, fragile, and air-sensitive films. The ability of SPM to observe their formation, evolution, morphology, and electrical and mechanical properties can contribute to the fundamental knowledge of SEI/CEI and the development of future battery systems. SPM has been extensively used to characterize the SEI, including its morphology and formation with *in situ* AFM[11–14] and its mechanical properties with extended AFM techniques[15–17].

2.2. Beyond Li-Ion

Recently, a number of "beyond Li-ion" systems have seen significant research focus; these include solid electrolytes, sodium-ion batteries, and batteries with pure lithium or sodium metal anodes. The implementation of these technologies could significantly improve the safety, sustainability, and energy density of rechargeable batteries.

Solid electrolytes mitigate the safety concerns associated with highly flammable organic liquid electrolytes and allow some simplification of battery design by eschewing the need for a polymer separator to physically separate the electrodes[18]. Solid electrolyte materials can consist of an inorganic material, generally an oxide or sulfide, a gel polymer containing a mix of liquid solvent and solid polymer matrix, or a fully solid polymer capable of solvating alkali metal salts. Each of these have their own drawbacks; the inorganic solids can be quite fragile and have poor compliance with electrodes undergoing volume expansion, leading to significant charge transfer resistance at the electrode-electrolyte interface, while the ionic conductivity of the polymer electrolytes is lacking compared to their organic liquid and inorganic solid counterparts. Composite solid-state electrolytes with a mix of crystalline inorganic and polymeric components can make up for these shortcomings, but further research is required to continue improving their ionic conductivity and understand their ion conduction mechanisms[19]. The ability of SPM to acquire localized nanoscale mechanical and electrical information makes it well-suited for analysis of the charge transport/transfer mechanisms and degradation of solid electrolytes, advancing understanding of their physiochemical properties and guiding future material design.

Sodium-ion batteries (SIBs) present a more sustainable alternative to LIBs due to the high abundance of sodium[20] and its relatively widespread geographic distribution[21]. The development of LIBs and SIBs began nearly simultaneously, with many similar characteristics between the two systems.[22] The electrode potential of sodium is close to that of lithium (-2.71 V for Na/Na^+ vs. -3.04 V for Li/Li^+), but sodium is both larger and heavier than lithium, giving it a disadvantage in terms of energy density[23]. As a result, LIBs reached commercialization sooner, "winning out" over the underdeveloped SIBs. Research on SIBs significantly slowed near the end of the 20th century following the initial commercialization of

the LIB, but has seen a significant revival in the past 15 years partially due to concerns about the sustainability and price of raw materials for LIBs[24]. Current LIBs use a significant fraction of high-cost copper, nickel, and cobalt materials; SIBs can instead use much cheaper and more abundant aluminum, iron, and manganese[25]. The lower energy density of sodium is less of a concern for fixed-location installations such as grid-scale energy storage than it would be for mobile applications; however, current SIBs continue to suffer from poor capacity and cycle life, necessitating further investigation into their operation and degradation mechanisms[20].

Pure alkali metal anodes would achieve the highest possible energy densities for their respective systems. The specific capacity of lithium metal (3,862 mAh/g)[26] is an order of magnitude higher than that of the commonly used graphite anode (372 mAh/g)[27]; as such, lithium metal has been referred to as the "holy grail" of battery anodes. However, alkali metal anodes are plagued by poor reversibility and stability, due in part to the inherent inhomogeneous morphology during plating/stripping. Lithium and sodium metal are also highly reactive and instantaneously form an SEI when they come into contact with most electrolytes[6]; dynamic morphological evolution over numerous cycles causes continuous generation of new SEI and corresponding consumption of electrolyte. Cracks in the SEI due to morphological change can become preferential deposition sites for cations, giving rise to even more inhomogeneous growth, which can create safety concerns from rapid dendritic growth and short circuiting[28]. SPM can be used to image the nucleation and growth of alkali metal deposits[29–31] as well as provide localized measurements of the surface potential, conductivity, and mechanical stiffness of the SEI covering alkali metal[29–32]. The insights gained from SPM analysis can be used to elucidate the relationship between electrolytes, SEI, electric double layer (EDL), interfacial charge transfer, and metal deposition/stripping, informing design of advanced electrolytes and artificial SEIs.

3. SCANNING PROBE MICROSCOPY TECHNIQUES

3.1. Atomic Force Microscopy

Foundational to nearly all advanced SPM techniques or modes is atomic force microscopy (AFM)[33]. Unlike STM, AFM can readily operate in either ambient conditions or fluid (including electrolyte solution) and does not require an electrically conductive sample or probe. In AFM, a sharp conical or pyramidal probe with radius of curvature on the order of a few (1-2) nanometers to microns is rastered across the sample surface (Fig. 3a). The tip is anchored to a cantilever, onto the backside of which a laser is focused and reflected into a position-sensitive photodiode. When the cantilever is deflected, the laser changes position on the photodiode, and the change in the resulting electrooptical signal is fed into a feedback loop to control a Z-axis piezoelectric transducer, enabling monitoring of the force on the probe (based on the known spring constant of the cantilever) while simultaneously recording height information[3,34]. AFM can thus be used to obtain topographical data with extremely high resolution in both the XY-plane (few to tens of nanometers, limited by the probe radius) and Z-axis (sub-Å/atomic scale, limited by the noise floor). Rather than constantly keeping the probe in contact with the surface, which can damage both the sample and probe, modern AFM measurements generally use intermittent contact (i.e., tapping) based modes, in which the cantilever is oscillated near the surface by a piezoelectric actuator and shifts in one or more parameters (e.g., oscillation amplitude, frequency, or phase) are monitored and captured[3]. In either standard tapping or "non-contact" tapping mode, a feedback loop is employed to oscillate the probe near its natural resonant frequency at a fixed amplitude relative to its free space amplitude (the "setpoint" amplitude), and the shift in the resonance frequency or phase as the tip approaches and interacts with the sample surface is detected and recorded. The difference between these two modes lies in whether or not the probe is allowed to enter the repulsive tip-sample regime (standard tapping) or remains fully within the attractive tip-sample

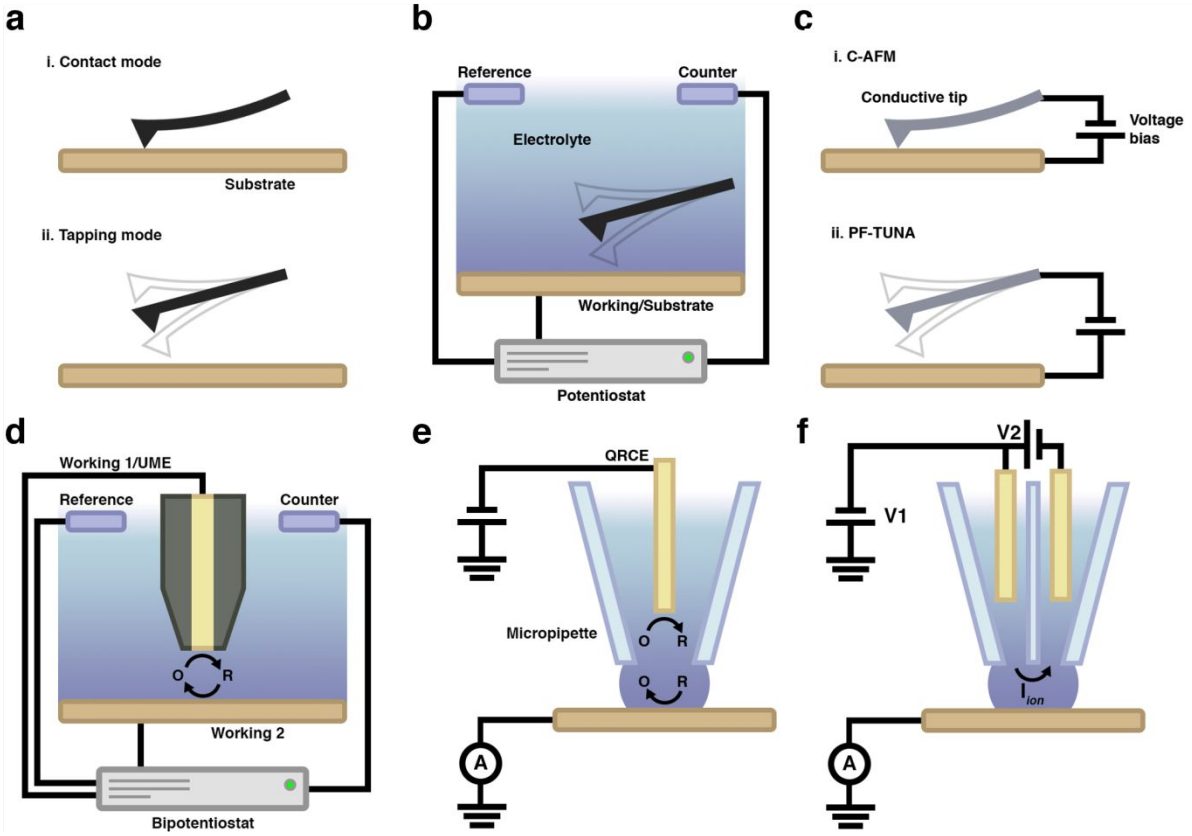

Figure 3. Schema of AFM (a) in contact mode (i) and tapping mode (ii), EC-AFM (b), the electrical SPM techniques (c) C-AFM (i) and PF-TUNA (ii), SECM in feedback mode (d), SECCM with a single-barreled pipette (e), and SECCM with a double-barreled pipette (f).

regime ("non-contact" tapping) throughout its oscillation. In PeakForce Tapping® mode, the probe is oscillated well below its resonance frequency and the maximum force exerted by the tip on the sample is the controllable parameter within the feedback loop, enabling acquisition of force-distance curves at kHz rates[35].

The plot of force on the probe (or cantilever deflection in units of nanometers or volts, all interchangeable via the spring constant and deflection sensitivity of the probe) against its separation from the surface, generally referred to as a force-distance curve or more simply *force curve*, can yield useful information about the mechanical properties of the sample (Fig. 4), including battery electrodes[36] and SEI. The slope of the linear region in the repulsive (i.e., contact) regime between the probe tip and sample, denoted by the region between points ***c*** and nearly to ***d*** in Fig. 4, can be used to

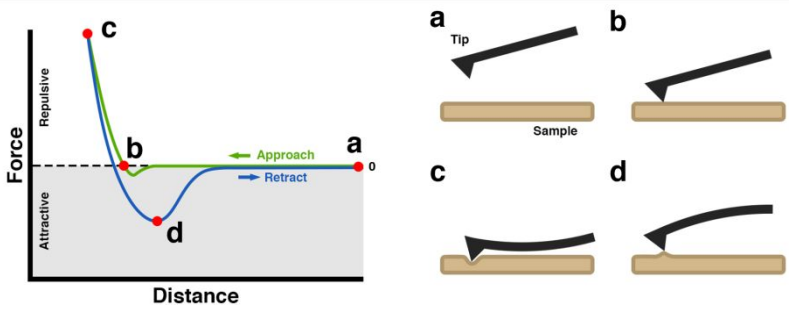

Figure 4. Left: An example force-distance curve acquired during a single approach-retract cycle. Right: Tip is far from the surface (a), engaged with the surface, but no force is applied (b), undergoing a repulsive force as it is pushed into the sample (c), and experiencing attractive force as it is lifted from the sample (d). Points a-d are indicated on the force-distance curve at left.

determine the reduced Young's modulus of the sample. The minimum force during withdrawal of the probe (i.e., maximum attractive force, indicated by point ***d*** in Fig. 4) quantifies the tip-sample adhesion[37], useful for determining SEI coverage due to the organic nature of many SEIs. Force curves can be generated during a slow tip approach-retract cycle or the force curves used to control PeakForce Tapping can be used to calculate the modulus at each pixel of an image, which is necessary for determining the heterogeneity of the SEI properties and composition. While these methods cannot directly yield chemical information, the modulus offers some limited insight into the composition, i.e., organic contents are generally softer, inorganic contents are harder.

Battery materials are often quite fragile and can be permanently damaged by the postmortem sample preparation necessary for characterization. In this case, *in situ* and *operando* methods are preferable. Electrochemical atomic force microscopy (EC-AFM) is a powerful *in situ/operando* measurement technique using a specialized cell to allow observation of changes in the topography of the electrode surface as a potential or current is applied to the electrode (Fig. 3b).EC-AFM on a battery electrode was first reported by Hirasawa et al.[38] in 1997, followed by Chu and coworkers a few months later[39], with both works involving *in situ* observation of the growth of SEI on highly-oriented pyrolytic graphite (HOPG) and other graphitic electrodes. EC-AFM has since been applied to study interphase formation and evolution in a multitude of systems (LIB, SIB, etc.), deposition and dissolution of Li metal, and volume expansion in electrode materials[12–14,40–45].

Despite the utility of EC-AFM, some limitations do exist. Both probe and cell materials must be resistant to the highly corrosive environment of liquid battery electrolytes, while also avoiding electrical interference, e.g., due to surface charge on the probe. The positions and sizes of the electrodes in a fluid EC-AFM cell must also be taken into consideration; since the surface of the working electrode must be available to be interacted with by the probe, the counter electrode may need to be positionally offset from the working electrode, potentially reducing the current density under the probe. The position of the probe in the diffusion path between the counter and working electrode can also artificially reduce the local current density. Designs for EC-AFM setups with solid electrolytes also exist, but in these cases, the position of the reference electrode needs to be carefully considered for accurate measurements. Finally, while AFM is not considered a destructive technique, caution should be taken when interpreting its results as its physical interactive nature can interfere with processes occurring on the surface of the sample. If excess force or tip velocity is applied during, e.g., a nucleation and growth process, some nuclei can be picked up and/or moved around by the probe if they are not large enough or have strong adhesion to the substrate, obfuscating the true nature of the process.

3.2. Electrical Characterization by Scanning Probe Microscopy

The high spatial resolution of AFM combined with the ability to employ conductive probes, either through coating of non-conductive probes with a metal or utilizing conductive materials such as doped diamond, enables a variety of SPM-based electrical characterization methods (Fig. 3c). Conductive AFM (C-AFM) is perhaps the simplest technique available to measure local electrical properties across a surface. In this method, a conductive probe tip is brought into direct contact with the sample to close a circuit as an external voltage is applied. As the tip is scanned across the surface, the current flow will change as the resistance of the sample changes, and variations in conductance or resistance across the sample surface can be mapped. In addition, the tip can be held at a static location and the voltage ramped to generate current versus voltage (i-V) curves. PeakForce Tunneling AFM (PF-TUNA™, Fig. 3c) is a variant of C-AFM based on the PeakForce Tapping® mode mentioned earlier using a conductive tip; because the tip is only in "contact" with the surface for a fraction of each cantilever oscillation, fast signal processing electronics can allow measurement of the resultant current flow without the use of contact mode, thereby preserving both the sample and probe tip. PF-TUNA is highly

sensitive, making it suitable for resistive samples such as solid electrolytes and SEI, and enables simultaneous collection of electrical and mechanical data[46]. These techniques can provide insight into the nanoscale heterogeneity of battery materials that would be challenging or impossible to obtain otherwise, having been used to analyze SEI properties and morphology[29,47] as well as the structure and transport properties of electrode materials[48–52].

Kelvin probe force microscopy (KPFM), or its simpler variant electrostatic force microscopy (EFM), can be used to observe local variations in modified work function[53,54]. When a conductive tip and sample are held in parallel tens of nanometers apart, an electrostatic force will arise between them due to their differing Fermi levels, observed as a flow of pseudocapacitive surface charge. In EFM, the resultant change in cantilever oscillation frequency or phase due to this tip-sample electrostatic force is measured to provide a qualitative map of variations in surface potential across the sample surface. In KPFM, the electrostatic force is instead nulled by applying a DC backing voltage to the probe or sample to minimize the electrostatic perturbation to the cantilever oscillation. The required backing voltage is then measured as the probe is rastered at a fixed height above the surface (based on the measured surface topography) to map the spatial distribution of variations in the modified work function. In order to quantify the sample's absolute work function, a reference material of known and stable work function (e.g., gold) must first be measured using the KPFM probe, and the reference material's theoretical work function subtracted from the measured tip-sample Volta potential difference (VPD) in order to find the work function of the tip for accurate and repeatable computation[3,55]. KPFM can operate in a few different scenarios in regards to battery testing. First, intermittent testing with VPD characterization (i.e., taking "snapshots") provides a progression of different materials properties, such as VPD of an electrode at different states and/or rate of lithiation[56] or the degradation processes over extended cycling[57]. Work function closely correlates to an electrode's open-circuit voltage and state of charge (SOC), allowing KPFM to approximate nanoscale SOC heterogeneity between or even within individual active material particles[58]. Additionally, KPFM has functioned as an *operando* tool, either in a cross-sectional observation of solid-solid interfaces during operation[57,59], or has been shown to function while in a humid environment, used in other research fields[60]. However, due to the metallic probe's own degradation when exposed to an electrolytic environment, this technique is currently incapable of *operando* measurements in a fully immersed condition. If conducting both KPFM and electron microscopy characterization of a sample, it is also important to consider the order in which those methods are employed, as exposure of the sample to the high energy electron beam may affect the measured Volta potentials[61,62].

3.3. Scanning Electrochemical Microscopy

Scanning electrochemical microscopy (SECM) is a useful tool for *in situ* study of localized electrochemical properties of a sample surface. In this technique, an ultramicroelectrode (UME) probe is brought very near to a substrate surface of interest and (depending on the mode used) a redox-active species in solution undergoes reduction or oxidation at the probe, substrate, or both, resulting in the transfer of electrons and flow of electrical current at the probe (Fig. 3d). This current is recorded by an external potentiostat as the tip is rastered across the sample at a fixed height or distance above the surface, allowing high-resolution (dependent on the radius of the UME) mapping of the electrochemical reactivity or chemical flux of the substrate; alternatively, a constant current can be maintained as the probe is rastered to map the topography of the sample.

SECM can be operated in several modes to obtain information about different systems. In feedback mode, the most common and versatile mode, the UME is biased at a constant potential and the sample substrate can be left unbiased or biased. The redox mediator near the probe undergoes either reduction or oxidation, generating a current that is then recorded. When the probe is very far away from the surface (d > ~2a, where d is the tip-to-sample distance and a is the probe radius), the diffusion-limited current is measured (Fig. 5a). As the tip is brought close to the substrate (d < ~2a), the tip current will be perturbed by the substrate due to its electrochemical reactivity. Taking reduction of the redox mediator at the UME tip as an example, when an O species is reduced at the UME to an R species, R can diffuse to the substrate when the tip is brought in the close proximity of the substrate. When the substrate is insulating, the diffusion of the redox mediator (O) from the bulk solution to the tip will be hindered and the tip current will decrease (*negative feedback*, Fig. 5b). If the substrate is conductive, R can be regenerated to O at the substrate and diffuse back to the tip, enhancing the tip current (*positive feedback*, Fig. 5c). By plotting the current as a function of tip-sample distance (often normalized to $L = d/a$), an *approach curve* is generated[63–65]. Approach curves are widely used to ascertain the electrochemical reactivity of a sample surface or a small area of the sample[66]. The mediator regeneration at the substrate is controlled by kinetics. Theoretical analysis of the approach curve can yield information on the electron-transfer reaction rate at the substrate. Feedback mode can also be used to make two-dimensional maps of the electrochemical activity of the sample surface by raster scanning above the surface and recording the current at each pixel, which has been used to observe SEI heterogeneity and change over time[67–69]. Since the measured current depends on both surface conductivity and tip-substrate separation in a constant height mode, rough or highly heterogeneous samples may have some obfuscation between the two factors. In these cases, hybrid AFM-SECM platforms may be employed to first scan the surface topography followed by an SECM scan that follows the line of the scanned topography. On the other hand, the probe can be kept at constant height during battery operation to observe the SEI evolution due to the surface conductivity changes, which is governed by SEI composition.

In generation/collection modes, both the tip and sample are electrically biased, causing different reactions to occur at each electrode. For example, in substrate generation/tip collection (SG/TC) mode, the substrate generates the electroactive species O, which is collected at the tip and reduced to R. SG/TC mode is frequently used for observation of reaction rates and chemical flux on the surface of a substrate, such as dissolution of transition metal ions from cathode materials[70–73]. Further information on SECM modes, probes, solvent systems, and operation can be found in Bard's original report of the technique[63], monographs on SECM[64,74], and a number of excellent reviews[75–77].

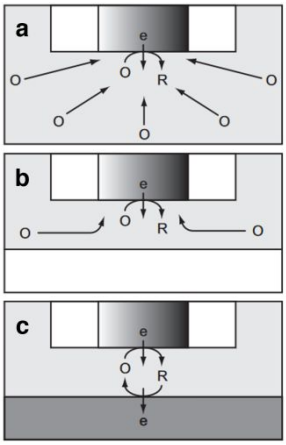

Figure 5. Mechanisms of SECM feedback mode in bulk solution (a), against an insulating substrate (b), and against a conductive substrate (c). Reprinted with permission from ref[65].

3.4. Scanning Electrochemical Cell Microscopy

Scanning electrochemical cell microscopy (SECCM) is a related technique utilizing a quasi-reference counter electrode (QRCE)-containing pipette that forms an electrochemical cell with the sample surface using a small droplet of electrolyte in meniscus contact[78]. Other electrochemical SPMs require the entire probe and sample to be fully immersed in the electrolyte solution, often necessitating a specialized sample cell. For each

experiment, the entire sample is utilized, even if only a small area of the sample is under observation. SECCM's ability to conduct a "new experiment" at dozens, if not hundreds, of locations on the sample allows statistically relevant quantities of data to be acquired in a short amount of time. This ability to conduct independent electrochemical processes, such as SEI formation and de/intercalation of ions at individual particles of electrode material[79–81], at unique locations can be used to obtain information about the heterogeneity of battery materials. In addition, the resolution of SECCM is improved over other techniques such as SECM.

The simplest form of SECCM uses a single-barreled pipette moving in a "hopping" motion (Fig. 3e)[82]. When the pipette is far from the substrate and the substrate is not in contact with the electrolyte, current is unable to flow because redox cannot take place at both electrodes. As the Z-axis piezo steps down to bring the probe towards the surface, the droplet meniscus is eventually formed between the pipette and the substrate. At this point, if the substrate is conductive, redox can occur at both electrodes and current is able to flow. Once current is detected, the probe is considered to be in "contact" and the Z-piezo is held at its same position. The extension of the Z-piezo can be recorded as the sample height, allowing for measurement of sample topography.

In double-barreled pipette SECCM, a double-barreled pipette containing two channels that are both filled with electrolyte is employed, with each barrel containing a QRCE (Fig. 3f)[78]. A passive voltage is applied between the two QRCEs, causing the flow of ions between the QRCEs through the droplet at the end of the pipette. The probe is subjected to a sinusoidal oscillation with amplitude a fraction of the pipette end radius. Once the droplet meniscus is formed with the substrate, an alternating (AC) current occurs between the QRCEs as the droplet shape is changed by the sinusoidal oscillation and the probe is considered to be in "contact." Once the probe is in contact, a voltage can be applied between the substrate and the QRCEs to conduct electrochemical operations. One benefit of using the double-barreled setup is that a conductive substrate is not required, since the AC ionic current between the two barrels is the signifier of contact rather than the current response between the substrate and QRCE. Several reviews focused on SECCM are available[83–85].

4. ELECTRODE-ELECTROLYTE INTERFACE

4.1. Electrode-Electrolyte Interphases

The SEI layer is one of the most important components of LIBs yet a challenging system to study due to its thinness (tens of nm), mechanical fragility, instability against air and moisture, and complex nature. SEI has previously been modeled as a "mosaic" of nanoscale organic and inorganic phases with a heterogeneous distribution through the depth of the SEI[86,87]. With the advancement of computational modeling and increasing adoption of *in situ* and *operando* methods, the understanding of SEI has continued to evolve[88–90]. In recent years, significant research attention has been focused on not only analyzing the process and result of SEI formation but also tuning the SEI towards more desirable properties. SPM techniques are useful for studying interphase layers because of their high lateral and depth-wise resolution, ability to obtain a variety of information (morphological, mechanical, electrical), and the potential for *in situ* and *operando* observation of interphase formation and evolution. With the use of SPM to characterize SEI properties, a more complete illustration of the complex relationship between electrode surface property, electrolyte composition and concentration, SEI composition and properties, and battery performance can be made.

Effect of electrolyte composition. Modification of the electrolyte is an essential aspect of the research push towards SEIs with superior properties for high performance batteries, but there is still significant understanding yet to be achieved about the SEI formation mechanisms of different electrolyte components. *Operando* EC-AFM and PeakForce quantitative nanomechanics (PF-QNM) are

two popular techniques used to study the effects of electrolyte composition on SEI formation, morphology, and mechanical properties. Observations of SEI formation from ether-based electrolytes[91–97], ionic liquids[98], water-in-salt electrolytes[99], and additives such as $LiNO_3$[95] and fluoroethylene carbonate (FEC)[100,101] have been performed. Zhang et al. reported the effects of FEC and vinylene carbonate (VC) additives on the SEI on highly oriented pyrolytic graphite (HOPG), showing that adding VC alone increases the SEI modulus on the basal plane while adding both FEC and VC improves both the modulus and homogeneity[102]. FEC and VC are known to increase the presence of LiF and crosslinked polymers in the SEI, respectively, increasing the modulus of the SEI. The increased homogeneity is likely due to the dense SEI initially formed in the presence of FEC, which offers superior protection against further SEI formation across a larger area of the anode. Graphite electrodes cycled in coin cells quickly form a resistive SEI in the presence of FEC and VC, yielding superior capacity retention and Coulombic efficiency through 20 cycles when compared to the additive-free electrolyte and electrolyte with only VC added. When only VC is added, the capacity drops quickly within the first 5 cycles, which the authors correlate to sluggish ion transport in the VC-derived SEI, supported by EIS measurements. The nanoscale resolution of SPM enables analysis of SEI's heterogeneity of morphology and mechanical properties, more fully completing the picture of the relationship between electrolyte composition, SEI properties, and battery performance in a way that other techniques cannot. Supplementary measurements of conductivity spatially using PF-TUNA or SECM could further improve this understanding at the nanoscale rather than relying on bulk methods such as EIS.

Tao et al. discovered that ethylene carbonate (EC)/dimethyl carbonate (DMC) electrolytes with 2 vol% FEC can completely prevent Na^+ ion intercalation into hard carbon (HC), while the FEC-free electrolyte allows ion intercalation; switching electrolytes in the same cell allows the ion intercalation "gate" to be closed and opened successively[103]. *In situ* AFM studies revealed that the dynamic dissolution and regeneration of Na-SEI plays a role in this selective ion transport mechanism. When the electrolyte is switched from FEC-containing to FEC-free, the NaF-rich SEI formed in the presence of FEC dissolves within a handful of cycles and a new, NaF-poor SEI allows ion intercalation to occur. While the instability of Na-SEI has been previously determined electrochemically[104–106], the AFM characterization in this work is a direct observation of the continuous dissolution and regrowth of individual Na-SEI particles. This reversible ion gate-switching mechanism of SEI can be used to inform future electrolyte designs for tunable SEIs. It should be noted that the SEI dissolution and regrowth in this work occurred when switching between two electrolytes; direct AFM measurements of SEI dissolution have not yet been reported in the *same* electrolyte over a long period of time. Because of the ability of AFM to function in a wide range of environments, it is well-suited for observing differences in SEI formation between electrolyte systems, providing new insights into the relationship between electrolyte composition and SEI morphology and properties.

Effect of the nature of electrode surface. The nature of the substrate material can also significantly affect the composition and morphology of the SEI. Along with mentioned work by Zhang, they characterized the differences in SEI formation between HOPG and a commercially relevant graphite particle, reporting that the higher edge-to-basal ratio of the commercial graphite resulted in a softer, thicker SEI than on the HOPG because of edge planes' higher electrochemical activity towards SEI formation[102]. This result highlights the necessity of studying industrial electrode materials (rather than purely relying on idealized substrates such as HOPG) in order to fully understand SEI formation in realistic batteries.

Zhu et al. elucidated the role of graphite surface defects in SEI formation by *operando* EC-AFM/PF-QNM of the morphological and mechanical properties of SEI formed on HOPG and on a defect-rich carbon material[107]. The onset of SEI formation on the defect-rich material occurred around 1.5 V (vs. Li/Li^+), notably higher than the onset potential for the HOPG basal plane (below 1.0 V). The SEI formed on the defect-rich material was found to be thinner, possess higher modulus, and passivate the surface

more effectively compared to the SEI on HOPG; these properties and the early onset of SEI formation are likely due to lower adsorption energy barrier of the EC solvent molecule bonded Li compound on a graphite surface with common point defects (e.g., Stone-Wales and single vacancy), and thus a more positive onset potential. Accompanying XPS results show a higher fraction of inorganic components on the defect-rich carbon material, in contrast to the aforementioned work of Zhang et al. showing that a thicker, softer SEI that implies a more organic nature is formed over graphite defects, e.g., edge planes[102]. This demonstrates one limitation of EC-AFM—it cannot directly observe chemical nature (instead making a relation to mechanical properties) or *in situ* nanoscale conductance as SECM/SECCM can. The step edges in HOPG and commercial graphite have different physicochemical behavior from the point defects that dominate Zhu and coworkers' defect-rich material, leading to different SEI formation and composition. Because mechanical properties can only act as a proxy for general composition (organic vs. inorganic), chemical analysis by surface-enhanced Raman spectroscopy (SERS), tip-enhanced Raman spectroscopy (TERS), or Time-of-flight secondary ion mass spectrometry (ToF-SIMS) should be used in concert with EC-AFM and SECM or SECCM in order to fully characterize the nature of the defect sites and the consequent SEI formation.

The effect of surface characteristics on SEI has also been studied by SECCM on several grades of HOPG with varying frequency and height of step edges[81]. The high-throughput SECCM enabled CV scans to be run at hundreds of points on each surface, revealing that more and larger step edges greatly improve the passivating ability of the SEI because of the significant initial SEI formation at step edges. These works utilize SPM to enhance understanding of the significant role played by the electrode surface in SEI formation and properties, showing that defect-rich graphites may be more desirable than pristine materials for improved SEI properties and could increase the (currently quite slow) speed of SEI formation in LIB manufacture by requiring fewer and/or faster cycles to reach an adequately passivating condition. SPM tools are ideal for study of these materials due to their ability to observe nanoscale morphological defects such as step edges as well as highly local characterization of SEI thickness, modulus, and passivating ability.

HOPG and carbon materials are the most commonly studied samples for SEI formation due to the ubiquity of carbonaceous electrodes such as graphite, but SPM studies on SEI of many different substrates have recently been reported: Li metal (on Cu or otherwise)[29,94,95,108], Si and Si compounds[109–111], Cu[112], and black phosphorus[113]. Martín-Yerga et al. used SECCM to statistically analyze SEI formation and cycling behavior of Si while altering the cutoff voltage and electrolyte solvent system. When colocalized with shell-isolated nanoparticles for enhanced Raman spectroscopy (SHINERS), it was observed that the SEI on Si is constantly dissolving, regenerating, and evolving, in contrast to the relatively stable SEI on graphite after the initial formation process[111]. SECCM observation has also shown that the surface conditions of Si have a significant effect on the SEI properties; when the native oxide (SiO_x) of Si is etched off with HF, the current response is significantly more heterogeneous and the SEI is less passivating, along with demonstrating inferior reversibility of lithiation and delithiation compared to SiO_x/Si. The native oxide layer blocks some reactions of electrolyte decomposition products with the Si surface, while the surface hydrogen termination of HF-etched Si provides a barrier to Li^+ intercalation and deintercalation[110]. The significant heterogeneity in current response may be due to variation of surface properties, either inherent to the Si surface or resulting from the HF etching process. Colocalization with secondary ion mass spectroscopy (SIMS) allowed the assessment of chemical signature at each SECCM site, showing that the electrochemical heterogeneity in the HF-etched Si also resulted in heterogeneity of the SEI chemistry: SECCM sites with higher current response had SEIs with a higher incidence of Li^+ and F^- at the exterior layer of the SEI. The ability of SECCM to perform large numbers of electrochemical operations on the same substrate in a short time makes it a highly valuable technique for analyzing the heterogeneity of battery materialsand the effects of different cycling protocols. Colocalization with nanoscale chemical analytical techniques can provide further insight into

the nature of SEI heterogeneity and the effects of surface heterogeneity on SEI properties, providing guidance for material synthesis and manufacture.

Mechanical characterization of SEI. AFM is an ideal tool for probing the mechanical properties of SEI. It has extremely high resolution for analysis of nanoscale heterogeneity; it physically interrogates all species in the sample as opposed to only measuring the long range order of crystalline (in X-ray diffraction) or Raman-active species; and it can be performed *in situ*, avoiding dehydration of the SEI that may change the composition and properties. A more in-depth comparison of AFM to other mechanical characterization methods can be found in a recent review[114]. Slow nanoindentation-style ramps can be performed to acquire hundreds of force curves in a short period of time, or PF-QNM mode can perform simultaneous topographical and mechanical measurements for mapping of the adhesion and modulus during an image scan. The Young's modulus of the SEI has been considered an important mechanical property due to frequent correlation of high modulus to favorable cycling performance[91,95,101,115], especially in lithium metal batteries as the strong SEI is said to suppress dendrite growth. However, SEI can take many different structures with differing degrees of depthwise heterogeneity; with such structural and chemical complexity, this relatively simple quantity seems insufficient to fully characterize the mechanical properties of the SEI. In addition, several parameters used to fit force curves for determination of the modulus often go unreported, harming reproducibility in the field. Further analysis of force curves and development of new techniques have recently been used to enhance understanding of the structure and mechanical characteristics of SEI, as well as to aid in the design of new SEIs[92–94].

Wang et al. analyzed force curve features of Li-based SEI on copper electrodes to elucidate layered SEI structures[92]. Potentiostatic holds at various potentials gave rise to SEIs with characteristics corresponding to different layered structures, including fully inorganic, layered organic-inorganic, and multilayer inorganic-organic-inorganic SEIs, determined by the slope and shape of the force curves (Fig. 6 a-h). The multilayer inorganic-organic-inorganic SEI formed at multiple different potentials was found to provide the best cycling performance in a Li-Li symmetric cell, exhibiting stable overpotential less than 50 mV for 800 cycles at 1 mA cm^{-2}, as well as when cycled against $LiFePO_4$, retaining 85% of its initial capacity after 280 cycles. The authors attribute this to the ability of the inner inorganic layer to suppress dendrite growth while the flexibility of the organic middle layer is retained. Full analysis of the force curves acquired by SPM (rather than simply deriving the modulus and adhesion) yields a more in-depth understanding of the multilayer nature and mechanical properties of SEI, highlighting possible future design strategies for SEI on Li metal anodes.

The use of mechanical parameters other than Young's modulus has also been proposed. Gao et al. showed derivation of the maximum elastic deformation energy that can be stored by the SEI (denoted by *U*), corresponding to the area under the force-displacement curve prior to its elastic strain limit, using a two-step nanoindentation procedure[94]. The first indentation (approach-retract) is done with a low force limit to ensure only the elastic region is sampled to obtain Young's modulus (then corrected for the underlying hard substrate), and the second test is performed with significantly higher force to cause SEI fracture for determination of the elastic strain limit. These parameters are then used to calculate *U.* In Li/Cu half cells tested with different electrolytes, *U* demonstrates clear correlation to the average Coulombic efficiency where the Young's modulus and elastic strain limit do not. The SEI formed in LiFSI in ethylene glycol diethyl ether (EGDE) has the highest average Coulombic efficiency of 98.44% under 1 mA cm^{-2} for 700 cycles and 99.04% under 3 mA cm^{-2} for 300 cycles along with the highest value of *U*, 43.97 pJ, among tested electrolytes. SEI derived from LiFSI in 2-methyltetrahydrofuran (METHF), with much lower Young's modulus, higher elastic strain limit, and slightly lower *U* than the EGDE electrolyte, maintains an average 98.66% CE at 1 mA cm^{-2} for 650 cycles, but fails in less than 70 cycles under 3 mA cm^{-2}. When paired with Sn alloy anodes, the electrolyte that generates an SEI with higher *U* again corresponds to superior performance, yielding stable discharge of

685 mAh g^{-1} over 200 cycles. The other electrolytes, utilizing LiFSI in dioxolane (DOL)/dimethoxyethane (DME) and EC/DMC, have notably lower *U*-values and demonstrate highly unstable cycling, failing around 100 cycles[94]. These works raise questions as to the utility of Young's modulus as the *only* reported value for SEI mechanical properties while showing the ability of SPM to perform alternative characterization of mechanical properties, which can be used to guide future electrolyte design and SEI formation protocols.

Characterization of *U* can be performed with nanoindentation-style force curve acquisition, but may not be suitable for fast mapping during image scanning as 1) two scans would be required to acquire the two different properties needed (Young's modulus and elastic strain limit) at each pixel and 2) the high force on the probe required to fracture the SEI and determine the elastic strain limit could cause surrounding SEI to also be fractured and possibly picked up and moved around by the probe,

obfuscating the true nature of the SEI. However, the force curve-based approach may also be eschewed entirely in favor of a new "nano-rheology microscopy" technique used to ascertain the shear modulus *G* and viscosity *η* in 3D throughout the SEI[93]. This technique utilizes a laterally oscillating tip that penetrates the sample while the in- and out-of-phase components are measured and used to calculate *G* and *η*. Independently measuring these parameters and plotting them against tip-sample distance allows the determination of different regions of SEI, namely organic-dominated layers with non-zero viscosity and shear modulus and inorganic-dominated layers with near-zero viscosity but positive shear modulus. Repeated measurements taken over a grid allow the generation of a high-resolution 3D map of SEI regions. Using this method, the SEI formed on the edge plane of HOPG was found to possess the classic organic-inorganic bilayer structure with a higher proportion of organic components than the

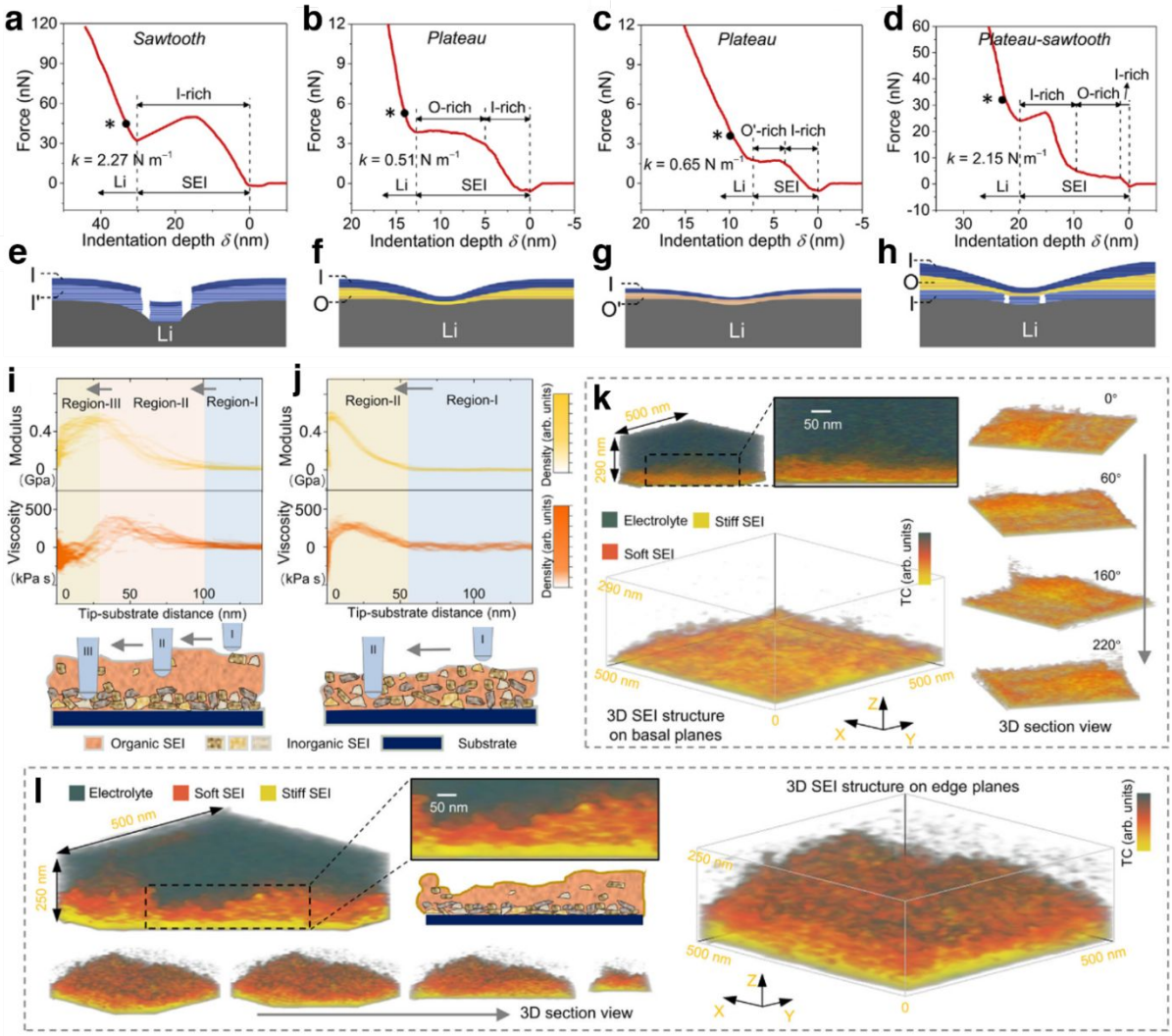

Figure 6. Force curves (a-d) and schemes of corresponding layer structure (e-h) for SEIs with different layering. (a-h) reprinted with permission from ref[92]. Copyright 2020 Elsevier. Distribution of shear modulus *G* and viscosity *η* through the depth of the SEI during nano-rheology microscopy, with schemes of tip-SEI below, for edge plane (i) and basal plane (j) HOPG. 3D map reconstructed from depthwise *G* and *η* distribution of the SEI formed on basal plane (k) and edge plane (l) HOPG. (i-l) reprinted with permission from ref[93]. Copyright 2023 The Authors.

basal plane SEI, which appeared as a mixed organic-inorganic layer with significant lateral heterogeneity (Fig. 6 i-l), in good agreement with XPS results. Based on this and the swelling of graphite step edges, which is easily observed by *operando* AFM, the authors suggest that the higher proportion of organic components on the edge plane SEI is due to the reduction of cointercalated solvent molecules, which is impossible through the basal plane. This also further explains the different (thin, highly inorganic) nature of the SEI on Zhu's point defect-rich graphite material, which is composed of different type of defect. This innovative new technique allows for more accurate determination of the 3D structure of SEI, potentially providing new insights into the role of SEI heterogeneity and layering in the cycling properties of battery electrodes. Future colocalization with high-resolution chemical characterization methods such as time of flight (TOF)-SIMS and electrical SPM techniques could greatly enhance understanding of the correlation between SEI chemistry, structure, and mechanical and electrical properties.

Adhesion is another nanomechanical property that can be utilized to track heterogeneity and correlate it to reaction mechanisms. Kitta et al. correlated a contrast in growing dendritic protrusions with their adhesive interaction with the AFM probe[30]. This revealed an influence on the physical state of a protruding surface by the electrochemical reactions. This was seen both while under galvanostatic conditions to examine surface reactions and during open circuit potential to further understand interphasial stability. The different nanomechanical properties are useful to examine surface behavior under different conditions, furthering understanding of the driving forces and failure mechanisms of different battery materials.

Cathode-electrolyte interphase (CEI). Interphases can also form at the cathode operating at high potentials, at which oxidative decomposition of electrolyte occurs, forming a CEI. The CEI is generally thinner than the SEI and is more difficult to image, even by highly sensitive SPM tools. It can also be accompanied by gas formation that causes issues when using *in situ* fluid cells, including encapsulation of the probe tip within a gas bubble or disruption of the optical path of the laser. Nevertheless, *in situ* EC-AFM imaging of CEI formation has been performed on solid-state cathodes[116,117] and on cathode materials in liquid electrolyte[44], including by Chen et al., who were able to clearly visualize a sheet-like CEI on $Li_{1.14}Ni_{0.13}Co_{0.13}Mn_{0.54}O_2$ (LMR) in the presence of a highly fluorinated electrolyte (HFE)[118]. The standard carbonate electrolyte did not form a visible CEI, instead primarily oxidizing to unstable organic fluorophosphates and generating significant amounts of CO_2 gas. This corresponded to extremely unstable cycling performance, with a precipitous drop in capacity around the 30th cycle culminating in less than 50 mAh g^{-1} discharge capacity at the 100th cycle, while the HFE exhibited enhanced cycling performance, delivering 250 mAh g^{-1} (85.5% of its initial capacity) after 100 cycles. Notably, standard laminated electrodes were used in this experiment rather than an idealized material that may not represent a realistic battery system. The appearance of the CEI formed from the HFE was easily ascertained in this case due to its relative thickness, but CEI formation by other electrolytes may not be so easily determined. For example, a 10 nm layer of interphase particles may be easily noticed on a nearly atomically flat graphite basal plane, but may be significantly harder to observe on cathode particles multiple microns in diameter, even after lamination and calendaring and with appropriate image processing. In this respect, further sample preparation such as cross-sectioning by ion milling may need to be employed to create flatter cathode samples for *in situ* study.

4.2. Alkali Metal Deposition

Significant interest exists in the utilization of pure lithium and sodium metal as anode materials because they theoretically allow 100% of the mass of the electrode to be used in the cell reaction, circumventing the capacity penalty caused by the "dead weight" host material of intercalation electrodes[119]. However, as covered in section 2.2, alkali metal anodes are currently plagued by poor

reversibility due to inhomogeneous deposition and continuous SEI generation. There exists limited understanding of the plating and stripping behavior of alkali metals and its relation to the electrolyte composition and SEI properties, especially its nanoscale heterogeneity that could lead to "hotspots" for alkali metal dendrites. SPM has proven to be a useful platform for study of these problems because of its high resolution, capability of functioning in a liquid electrolyte environment, and ability to acquire nanoscale mechanical and electrical data mapped to the morphology. For example, Shi et al. observed the deposition and stripping behavior of Li and its leftover SEI shells in repeated cycles. They found that during the first stripping process, pitting appeared on the previously deposited particles, followed by total collapse of the SEI shell[108]. During the second deposition, fresh Li deposits preferentially nucleated in pristine areas of the substrate rather than refilling the collapsed SEI shells, likely due to the electrically insulating nature of the leftover SEI.

In situ AFM and QNM were also applied by Wang et al. to characterize SEI formation and Li deposition on HOPG hybrid intercalation/deposition electrodes in $LiPF_6$ and LiFSI-based electrolytes, showing that LiFSI is well-suited to homogenous Li metal plating/stripping but can hinder deintercalation of Li from graphite due to its highly dense SEI[120]. *In situ* EC-AFM was used to observe the morphology of SEI and plated/stripped Li metal at different capacities as well as the morphology of the HOPG electrode after stripping and deintercalation of Li. When greater than 3 mAh cm^{-2} of Li metal was deposited and stripped from the graphite electrode in the $LiPF_6$ electrolyte, AFM revealed significant exfoliation of the HOPG due to intercalation of Li, which caused the corresponding de/intercalation capacity to gradually diminish during cycling. In LiFSI electrolyte at 3 mAh cm^{-2}, Li plated as nanoparticles and, when stripped, left behind SEI firmly attached to the intact HOPG layers. However, the dense SEI gradually reduced deintercalation capacity over long cycling. When the plating capacity was reduced to below 3 mAh cm^{-2}, the hybrid electrode retained 97.6% of its initial capacity after 560 cycles, revealing the highly reversible Li metal plating/stripping in the LiFSI electrolyte and that the LiFSI-derived SEI only diminishes deintercalation under high plating capacity, possibly due to thick SEI formed at high Li deposition. These works provide morphological insight into the complex relationship between electrolyte composition, cycling protocol, SEI formation, and Li plating/stripping, which is challenging to obtain by other characterization methods that do not possess EC-AFM's extremely high resolution and *in situ* capability.

This understanding can be extended using *operando* AFM combined with a suite of *ex situ* electrical and mechanical characterization modes. In an experiment by Wang et al., *operando* AFM was used to observe the morphology of SEI formation and Li deposition at several current densities, with postmortem *ex situ* C-AFM and TUNA analysis performed (Fig. 7)[29]. At lower current density, a root-growth mechanism at the broad initial deposits was found to dominate; at higher current density, the initial small and homogeneous deposits gradually merged into larger deposits driven by a tip-growth mechanism, supported by *ex situ* C-AFM. TUNA revealed areas of high conductivity around the particle boundaries in the low current density regime and around the tip growth-driven protrusions in the high current density regime, both likely due to continuous SEI breakdown. Notably, the SEI formed under higher current density appeared to possess multiple layers of organic and inorganic composition, signifying its repeated fracture and regrowth during fast deposition. This application shows the capability of SPM to observe electrical properties with nanoscale resolution, offering unique insights into the growth regime of individual Li metal deposits and their relationship with SEI. Colocalization of

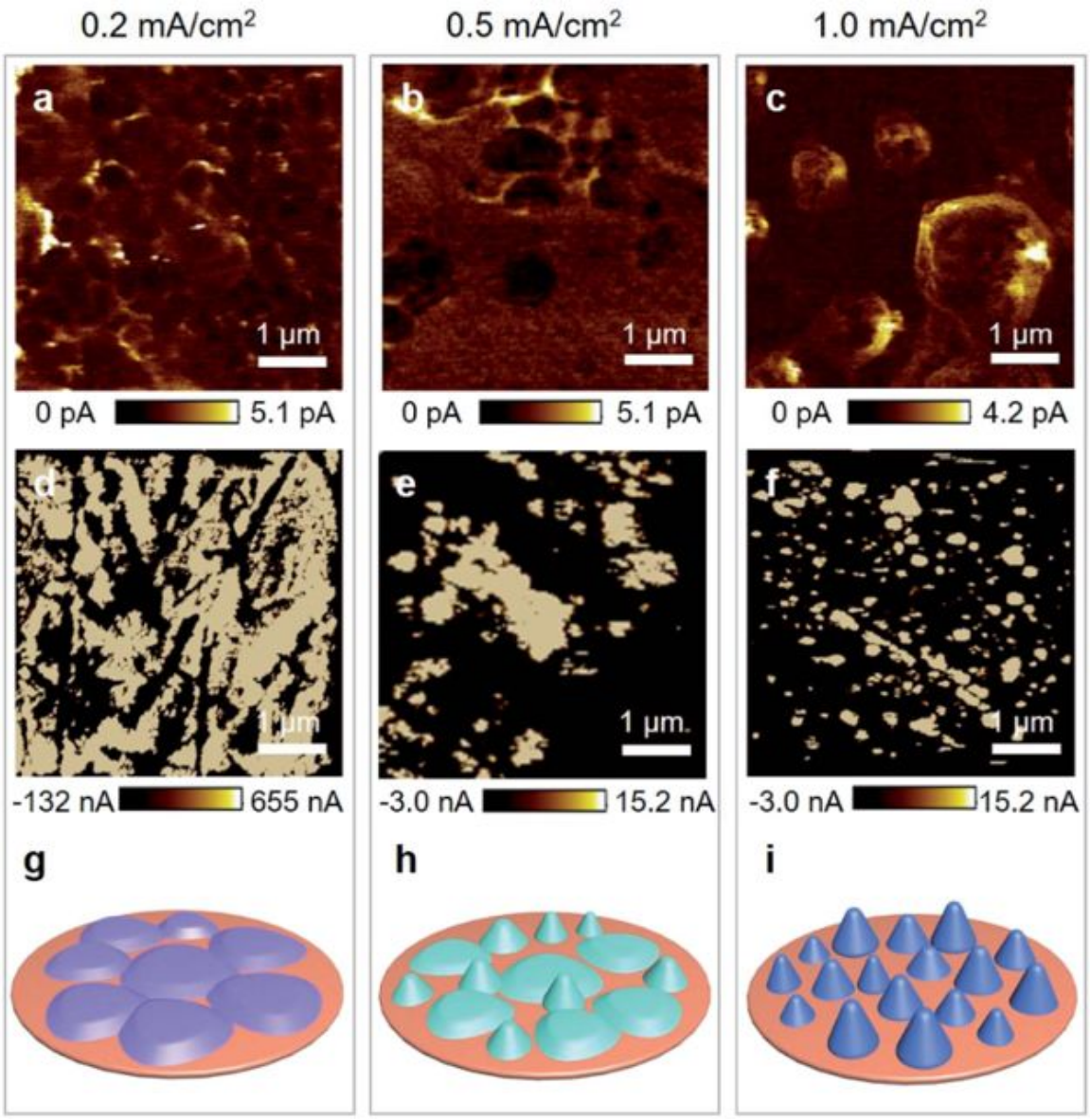

Figure 7. TUNA current maps (a-c), C-AFM current maps after scraping away the surface layer of Li (d-f), and scheme of Li morphology (g-i) following 1.0 mAh cm^{-2} Li deposition at 0.2, 0.5, and 1.0 mA cm^{-2}. Reprinted with permission from ref[29]. Copyright 2020 Royal Society of Chemistry.

multiple electrical SPM methods with different sensitivities allows in-depth investigation into these processes.

Rather than performing *operando* AFM in a liquid electrolyte, Liu et al. combined environmental TEM with AFM (ETEM-AFM) using a carbon nanotube attached to the tip to apply voltage, allowing simultaneous morphological, electrical, chemical, and mechanical characterization of Na growth under CO_2 atmosphere[121]. It was demonstrated that Na initially grows as a nanosphere regardless of the applied voltage, but the eventual morphology (whiskers, pillars, larger nanoparticles, faceted nanorods) is determined by the voltage. The tensile strength of the Na dendrites varies between 95-203 MPa, significantly stronger than bulk Na, while possessing significant internal stresses that can lead to creep

of Na in solid electrolytes. This work provides insight into the growth regime of Na dendrites and possible failure mechanisms in solid-state Na-metal batteries.

4.3. Solvation Structure

Solvation structure, or the arrangement and nature of the shell of solvent molecules that surround a dissolved cation or anion, has been receiving increasing attention over the past decade. Numerous publications, especially those involving high-concentration and localized high-concentration electrolytes, support a strong relationship between the molecules present in the Li^+ solvation shell and the eventual composition of SEI[122–125], while others focus on the role of the solvation structure in allowing intercalation/deintercalation of Li^+ ions regardless of SEI properties[126]. Ion solvation plays a key role in the operation of current battery systems, and improving understanding of solvation structure and its relation to ion transfer, SEI properties, and cycling stability will allow for rational design of future electrolyte and electrode materials[127]. Despite being typically used to study solid electrode surfaces, AFM is uniquely positioned to study the electrolyte itself due to its extremely high resolution in the z-axis (i.e. moving through the electrolyte toward the electrode surface). Other tools for analyzing solvation, such as Raman spectroscopy or nuclear magnetic resonance (NMR), yield chemical information but have much poorer resolution, making it challenging for them to only observe the interfacial region.

Ionic liquid electrolytes tend to form an ordered multilayer structure in proximity to a charged surface due to their inherent ionicity. This is shown in the work of Rakov et al., who used force curve analysis to observe the interfacial ordering phenomena of NaFSI in *N*-methyl-*N*-propylpyrrolidinium bis(fluorosulfonyl)imide (C3mpyrFSI)[128]. A number of periodic deflections with increasing amplitude are observed in the force curve as the probe approaches the surface, corresponding to the force required for the probe to "punch" through each charged layer as supported by MD simulations of the multilayer ordering. Electrolyte with 0-10 mol% NaFSI possessed four to five layered steps, while addition of 50 mol% NaFSI greatly reduced the number of steps and the rupture force required to penetrate each layer as the ions became less ordered. At this high concentration, Na^+ and FSI^- form extended aggregates near the electrode surface rather than participating in the layered structure with the $C3mpyr^+$ cation. When SEI is formed from these aggregates, enhanced interphasial chemistry results, especially under polarization at large negative voltage. A high-voltage precycling treatment (five cycles of 5 mA cm^{-2} to 0.1 mAh cm^{-2}) derived from the SPM observations applied to Na/Na symmetric cells with the 50 mol% NaFSI electrolyte enabled the cells to retain stable cycling at 1 mA cm^{-2} for over 700 cycles.

Bonagiri and coworkers have developed an SPM technique known as charge profiling three-dimensional atomic force microscopy (CP-3D-AFM) in order to ascertain the charge distribution of the electrode surface and the electric double layer at the electrode-electrolyte interface[129]. 3D force mapping is first performed at several potentials, recording the cantilever deflection as the probe is oscillated sinusoidally in the z-axis and is moved in the x- and y-axes. Count histograms as a function of z (obtained by integration of count distributions in x-z cross-sections) are then deconvoluted into charge density peaks and quantified using Poisson's equation $\nabla^2\varphi = -\frac{\rho}{\varepsilon}$, where φ is the potential, ρ is the charge density, and ε is the dielectric constant. Applying CP-3D-AFM to 21 m LiTFSI in water on an HOPG electrode shows significant peak separation increase as the electrode becomes more polarized (i.e. a more positive potential pushes the positive charge peak away from the electrode surface as the negative charge peak moves closer, and vice versa). At zero electrode potential (vs. Pt), the positive and negative charge density peaks nearly overlap. By finding the ratio of the areal charge density to the electrode surface charge density at the same potential, an "overscreening" effect in which the first layer of the EDL overcompensates for the charge of the electrode surface is revealed. Similar work has been

performed on 1-ethyl-3-methylimidazolium bis(trifluoromethylsulfonyl)imide (EMIM-TFSI) on HOPG and MoS_2 electrodes[130,131]. These works utilize SPM to provide crucial insight into charge-ordering phenomena at charged interfaces that are essential for electrochemical devices and can be used to inform design of electrolytes and charged interfaces in real systems.

Frequency modulation atomic force microscopy. Rather than directly observing cantilever deflection resulting from interfacial ordering, frequency modulation AFM (FM-AFM) is often used. FM-AFM is a non-contact AFM mode in which the resonant frequency shift of the probe is measured as a feedback signal. By measuring the frequency shift as a function of distance from the surface many times as the tip is rastered over the sample, 2D and 3D maps of the frequency shift can be obtained[132]. Bao et al. used FM-AFM to analyze the interfacial nanostructure of 1-ethyl-3-methylimidazolium bis (trifluoromethylsulfonyl)imide (EMI-TFSI) on lithium titanate (LTO) with and without additional LiTFSI salt[133]. 2D mapping in neat IL revealed the periodic distortion of the resonant frequency consistent with ionic ordering; however, when 1 wt% LiTFSI was added to the IL, the ordered interfacial structure disappeared due to continuous transfer of Li^+ to and from the substrate. The electric double layer structure in standard ionophoric electrolytes can also be studied by use of FM-AFM, as shown by the work of Yamagishi and coworkers[134]. Their study of the solvation of LiTFSI in PC at the interface with mica showed increasing spacing of ordered layers as the salt concentration increased, implying that the effective size of molecules at the interface increased (Fig. 8). While structural characterization of electrolyte solvation at the interface has previously proven difficult, SPM study supported by simulation is able to offer new insights into the solvation structure and guide future electrolyte design.

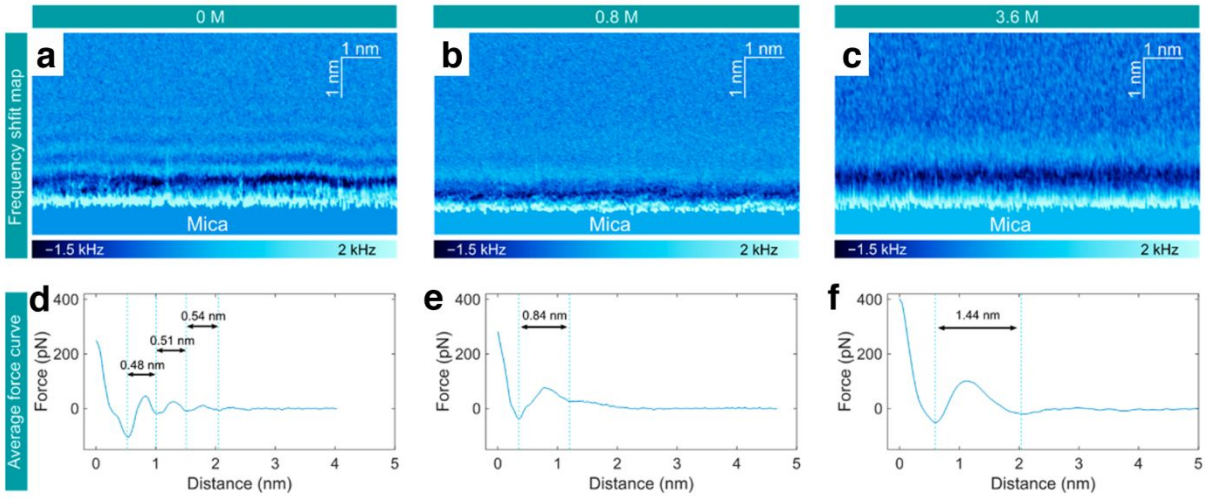

Figure 8. FM-AFM frequency shift maps of ordering of LiTFSI in PC of varying concentrations (a-c). Corresponding average force curves obtained from conversion of frequency shift data into force maps (d-f). Reprinted with permission from ref[134]. Copyright 2022 American Chemical Society.

5. CATHODE MATERIAL DEGRADATION

Although less common compared to studies of SEI or alkali metal deposition due to the significant roughness of laminated electrodes, SPM techniques have also been applied to study a number of intercalation and alloying electrodes as well as catalysts for Li-O_2 batteries, both *in situ* and *ex situ*. The most common use of SPM in the study of cathode materials is in understanding their degradation mechanisms, which is vital to improving their longevity and ability to operate at high

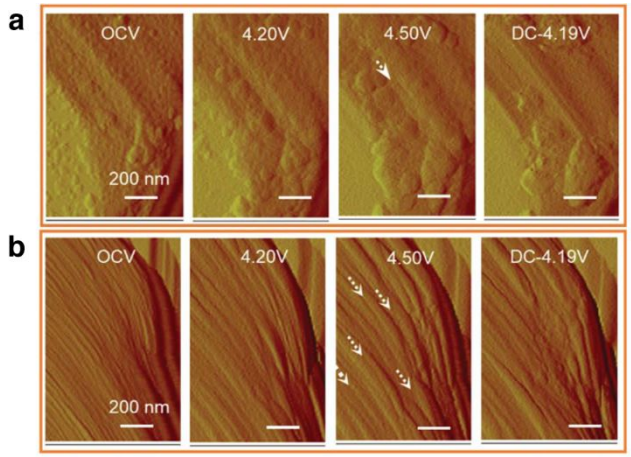

Figure 9. EC-AFM observation of planar gliding and microcracking under overcharge and discharge in two selected areas (a-b). Reprinted with permission from ref[137]. Copyright 2020 AAAS.

current or voltage: transition metal dissolution[70,72,73], lattice oxygen release[135,136], cracking due to phase transformation[49,137], and delamination of active material from its surrounding matrix[49,138] have all been evaluated by SPM techniques. These experiments often incorporate sample prep methods such as thin film growth, single crystal growth, and ion milling in order to create samples dimensionally suitable for SPM analysis from the top down or bottom up.

For example, Bi and coworkers synthesized single-crystal $LiNi_{0.76}Mn_{0.14}Co_{0.1}O_2$ (NMC76) in order to study the structural changes that occur during charge, overcharge, and discharge[137]. As the single crystals are charged to 4.2 V and beyond (4.5 V), partially reversible planar gliding and, eventually, fully irreversible external cracking are observed by *in situ* AFM as a result of shear stress from phase transformations (Fig. 9). This is reinforced by HRTEM showing internal cracking due to accumulated stress from over 100 cycles despite the planes generally recovering to their original positions. The high resolution of AFM makes it uniquely suited to analysis of structural changes resulting in nanoscale morphological changes such as planar gliding and microcracking; lower-resolution techniques may not be able to resolve the subtle morphological changes associated with these processes. SPM-assisted understanding of the crystallographic changes associated with high-voltage charging can aid in devising strategies to counteract it, allowing the realization of future high-energy density batteries.

Wu et al. examined a thin film $LiCoO_2$ cathode, which are extensively utilized in microelectronics[57]. They were able to effectively obtain a sample surface clear of contaminants, allowing intermittent "snapshot" visualization of the cathode as a function of cycling. With the use of KPFM and contact stiffness measurements, they saw a correlation between grain size enlargement, degradation of mechanical stiffness, and reduced surface potential over cycling. The degradation initiation was significant during the first 10 cycles, after which aging was less drastic as cycling continued. Researchers at Vrije University in Belgium were able to conduct similar intermittent examination of a $LiNi_{0.80}Co_{0.15}Al_{0.05}O_2$ (NCA) cathode at different states of charge[56]. They used a bootstrap method to correlate VPD to state-of-charge of the cathode surface, suggesting that sluggish solid-state diffusion of ions affects the electrode's capability to fully delithiate at increased rates. In these works, SPM plays a central role in advancing the understanding of the evolution of material properties resulting from long or intense cycling.

Ion dissolution from cathode materials. The ability of SECM to sample species released from the electrode material into the electrolyte solution makes it a valuable tool for the analysis of cathode degradation by ion dissolution. In work by Huang et al., a lithium manganese oxide (LMO) cathode was held at 4.5 V for 5 hours to induce dissolution of Mn ions, followed by CV performed at the SECM tip to determine the presence of electrochemically reactive species in the electrolyte (i.e., Mn ions)[72]. Experiments with different Li salt anions showed that $TFSI^-$ was found to greatly suppress Mn dissolution compared to PF_6^- and ClO_4^- owing to lack of HF and HCl formation, respectively.

Mishra and coworkers instead used SECM to study the release of oxygen from lithium cobalt oxide (LCO), NMC111, and NMC811 cathodes by applying a gradually positive-stepping potential to the cathode material and pulsing the tip potential between 1.3 V (at which oxygen reduction occurs) and 3.2

V multiple times during each cathode potential step, then averaging the tip current passed during oxygen reduction (Fig. 10)[135]. All three electrodes underwent a previously unseen transient O_2 release in the 2.9-3.4 V region in the first cycle, in addition to continuous release above 3.6 V. SECM analysis of multiple locations on the NMC111 electrode revealed significant spatial heterogeneity in the evolution of oxygen, highlighting the role of property and morphological heterogeneity in the degradation of NMC. Further experiments on basal plane and highly faceted LCO showed notable spatial heterogeneity in the degree of oxygen release regardless of crystallographic orientation, but few meaningful differences in net oxygen release between the basal plane and highly faceted specimens[136]. The authors propose that using a smaller ultramicroelectrode on the order of hundreds of nanometers may be necessary in order to directly probe oxygen release from individual facets of an LCO sample. These works highlight the unique power of SECM in observing previously unseen reactions and analyzing chemical pathways of cathode degradation.

Characterization by electrical SPM. Ex situ electrical SPM in the form of C-AFM and scanning spreading resistance microscopy (SSRM) can be used to analyze the conductivity of active material particles and differentiate the surrounding matrix from active material, yielding further information about cathode degradation. SSRM bears similarity to C-AFM in its use of contact mode and a bias voltage between the probe and sample, but is able to measure a wider range of currents due to the use of a logarithmic current-voltage converter[109]. These techniques have been used to observe the effects of ALD coating of Al_2O_3 on the conductivity of NMC electrodes, showing that the coating enables superior capacity retention due to preservation of particle conductivity after cycling[139], and for correlation of local conductivity to the morphology of NMC particles in a polysulfide solid-state electrolyte (SSE)[49]. These applications show the ability of electrical SPM to observe local property degradation in cathode materials, informing future strategies for preservation of conductivity and morphology.

6. SOLID STATE ELECTROLYTES

Solid state electrolytes (SSEs) are one of the most significant directions of research in the battery field. SSEs can take the form of solid polymers, gel polymers, ceramics, glassy materials, and composites of the aforementioned. These electrolytes boast improved safety over highly flammable liquid electrolytes as well as high mechanical strength that could aid in the suppression of the dendritic growth that plagues alkali metal anodes[140]. However, as previously noted, the ion transport mechanisms of many composite SSEs remain unclear. SPM is able to acquire localized nanoscale mechanical and electrical information, allowing it to play an important role in the analysis of these mechanisms as well as degradation of SSEs.

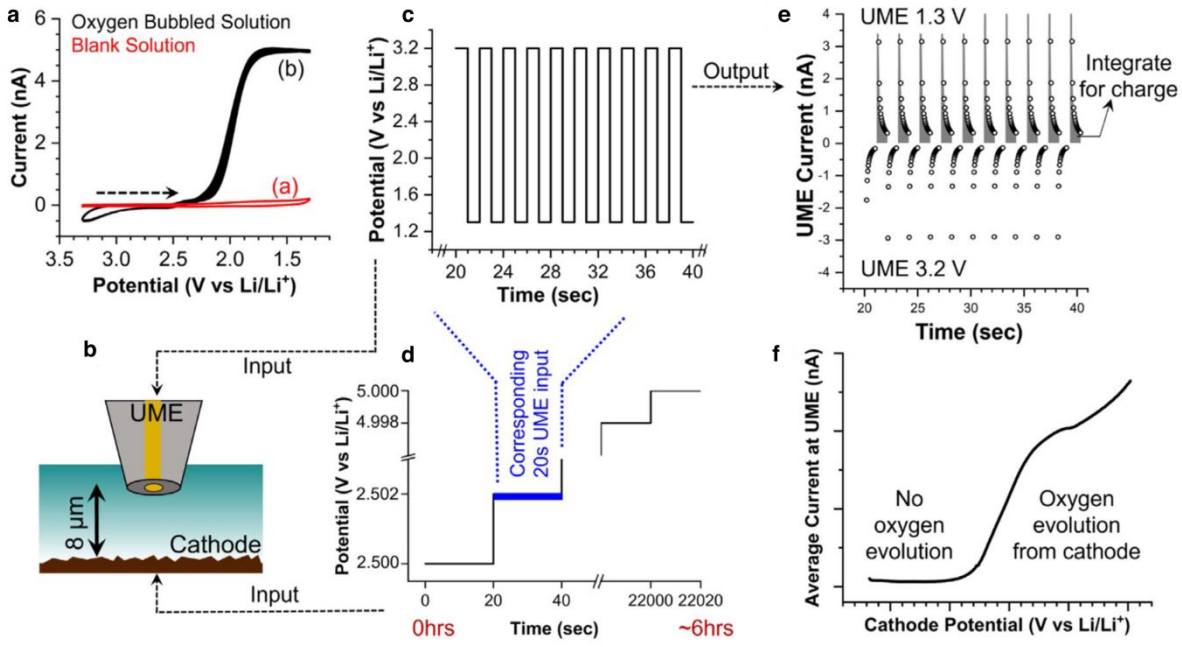

Figure 10. Determination of potential for oxygen reduction reaction (A). SECM experimental schematic (B), with input at the UME from (C) during a single step of (D), which is applied to the cathode material. The current output from the UME (E) and example plot of average UME current vs. cathode potential (F). Reprinted with permission from ref[135]. Copyright 2022 IOP Publishing.

Charge transport imaging. Composite SSEs typically incorporate ceramics possessing high ionic conductivity with flexible polymers that can achieve good interfacial contact between the electrodes and electrolyte. Shen et al. used AFM and QNM to characterize mixed $Li_{6.25}La_3Zr_2Al_{0.25}O_{12}$ (LLZO)/poly(ethylene oxide) (PEO) solid electrolytes with varying concentrations of LLZO at several increasing temperatures, using the topography, modulus, and adhesion data to map the distribution and morphology of each component[141]. A unique application of PF-TUNA allowed determination of the ionic conductivity in each region: when a positive bias was driven between the probe and sample, the system operated like a battery, with Li metal being oxidized to Li ions that then moved through the electrolyte towards the probe while electrons flowed to the probe externally, allowing sum measurement of ionic and electronic current (Fig. 11a). When a negative bias was driven, the probe was unable to return the flow of ions, allowing only the measurement of electronic current (Fig. 11b). Because the electronic current is orders of magnitude less than the ionic current in solid electrolytes due to their insulating

nature, the signal from the positive bias scan was used as the ionic current measurement. The SPM measurements showed that electronic conduction primarily occurs through PEO rather than through LLZO, while ions conduct through the amorphous PEO at high temperature and low LLZO concentration (Fig. 11i-l); as more LLZO is added, it forms a continuous matrix through which Li^+ prefers to migrate. A similar technique was used by Jiang et al. to characterize the degradation of a lithium-ion conductive glass ceramic (LICGC) electrolyte, showing a heterogeneous distribution of regions with differing degrees of degradation across the SSE surface owing to local compositional heterogeneity[142]. In these works, SPM's capability of analyzing nanoscale conductivity and its flexibility to adapt to different samples and processes are used to inform important conclusions about the ionic conduction and degradation mechanisms of SSEs.

Kelvin probe force microscopy. KPFM has also been useful for the observation of surface potential in SSEs. In combination with neutron depth profiling for mapping Li distribution, KPFM was used by Fuller et al. to ascertain surface potential across the width of a Si-lithium phosphorus oxynitride (LiPON)-$LiCoO_2$ (LCO) cell[143]. The contact potential can be correlated to the composition and potential of each layer of the cell. The sharpest drop in potential was found to occur at the anode-electrolyte interface, with a smaller drop occurring at the cathode-electrolyte interface and a shallow gradient existing through the bulk electrolyte. The Si electrode was found to undergo nonuniform lithiation and slow Li^+ diffusion, with a higher concentration of Li remaining near the electrolyte even after several

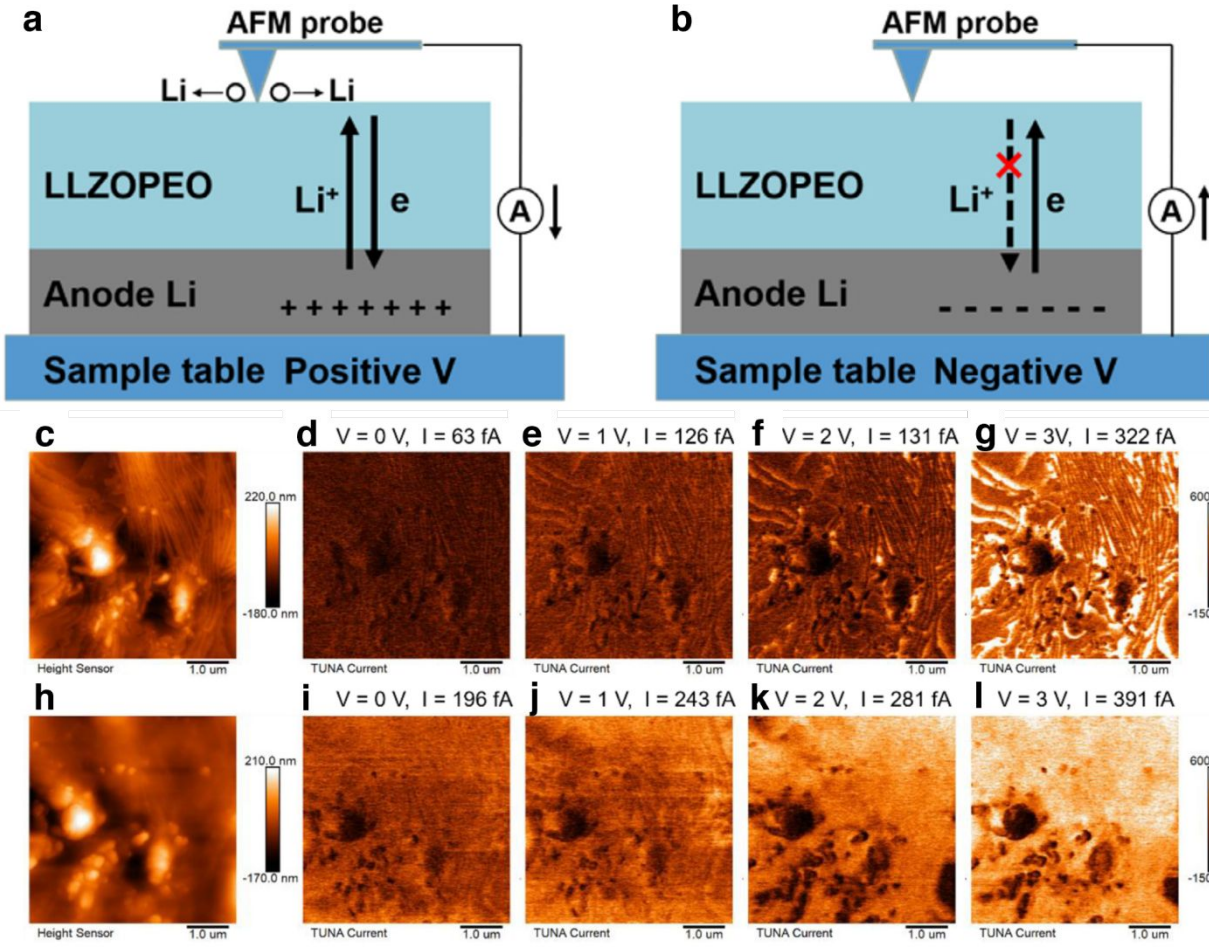

Figure 11. Scheme of the imaging setup for ionic and electronic current (a-b). AFM images of the topography (c) and Li^+ current (d-g) in 50 wt% LLZO-PEO/$LiClO_4$ at 50 °C. AFM images of the topography (h) and Li^+ current (i-l) in 50 wt% LLZO-PEO/$LiClO_4$ at 55 °C following PEO amorphization. Adapted with permission from ref[141]. Copyright 2021 Elsevier.

hours, confirmed by both KPFM and neutron depth profiling. Masuda et al. were able to examine the cross-section of a solid-state battery, to probe a cathode-electrolyte composite, which is one of the possible solutions to the high solid-solid interfacial resistance that plagues solid-state batteries. Here, KPFM was used to differentiate activity of separate phases within the composite during cyclic voltammogram operation[59]. Another key takeaway from this work was the temporal effects, where the probe has a limitation in its rate of providing data. If the probe scans at a rate slower than the actual evolution of reactions, and therefore measurable data from the probe, then there will be visible contrast that must be considered during *operando* testing. These publications highlight innovative uses of SPM and the versatility of extended SPM techniques to obtain a wide range of information about SSEs, informing future material design.

7. Summary and Outlook

We have reviewed recent advances of SPM to the studies of surfaces and interfaces in rechargeable battery systems, focusing on AFM-based methods as well as SECM and SECCM. Works involving SEI and CEI formation, lithium metal deposition and stripping, observation of ion solvation structures, cathode material degradation, and solid electrolyte materials have been highlighted. SPM has proven to be a highly effective family of techniques for observation of nanoscale morphology and local electrical and mechanical properties of battery materials, accessing new information concerning nanoscale property heterogeneity to inform future design of both liquid and solid electrolytes, SEI, and electrode materials. Information obtained from SPM has been used to implement new cycling protocols leading to increased battery lifetime, determine ideal electrode-electrolyte combinations to reduce degradation, and improve understanding of the relationship between electrolyte composition, SEI, and lithium metal plating and stripping morphology.

Works within the last several years highlight the increasing prevalence of colocalization and simultaneous characterizations, either using multiple SPM methods or SPM methods combined with other characterization techniques. There is also increasing adoption of *in situ* and *operando* methods such as EC-AFM and SECM due to their ability to more accurately characterize a battery material in more realistic environments and to observe the evolution of morphological, mechanical, and electrical properties of materials during electrochemical processes. This includes the expansion of SPM to new samples and dimensions, such as the study of electrolyte structure, CEI, and transition metal dissolution. These exciting works reveal information previously unobtainable or inaccessible by the more common electron microscopies and spectroscopic methods.

As implementation of SPM measurements becomes easier and more widespread, caution should be taken to ensure physically sound experimental configuration, accurate interpretation of experimental results, and detailed experimental methods for reliable and reproducible measurements.

- While relevant instrumental parameters are generally covered quite well in the experimental methods section, there is a general underreporting of methods used for the quantitative analysis of AFM force curves. The software used, tip-sample interaction model (e.g., Hertz, Sneddon, DMT, etc.) and calibration methods for the tip radius, spring constant, and deflection sensitivity should be reported in order to maximize reproducibility. If automatic fitting software such as AtomicJ was used, this should also be reported along with the relevant processing parameters. Additionally, sample force curves or all force curves overlaid upon each other should be shown with the data. If the force curves are complex, e.g., of a multilayer SEI with distinct features, analysis of those features should be performed[92].
- The role of tip-sample interaction and the fundamentals of electrochemistry must not be ignored. For example, during *operando* EC-AFM of SEI or alkali metal deposition there is the possibility of the AFM probe sweeping off some nuclei before they are able to grow to an

appreciable size and maintain adhesion with the substrate, resulting in artificially lowered nuclei density. It is imperative to cross-check the *operando* scanned area against a previously unscanned area to ensure that they are similar enough to be able to draw reasonable conclusions. In addition, some *in situ* cell hardware may offset the counter electrode and working electrode or otherwise alter the ion diffusion route between the electrodes, and consequently the concentration profile, which can artificially reduce the local current density in the scan area. EC-AFM cells may be commercial or homebrew, but in both cases the cell geometry should be reported.

- The transient state of the material being imaged must be taken into account. The time it takes to acquire data, a function of the lateral velocity of the probe and the resolution of the image, will impact this acquisition rate. If the reactions are occurring at a rate faster than this data collection rate, then information such as the scanning direction, voltage range during a scan, and other metrics should be provided.
- As most of the aforementioned battery operations are sensitive to air, the SPM measurements usually require the operation being performed under controlled environment, e.g., in a glove box. Cautions should be taken when applying SECM or combined AFM/SECM in such environment, as submicron and nanoscale probes could be damaged due to electrostatic discharge[144] which affects the interpretation of the results. Additional characterization such as SEM needs to be conducted to confirm the size and morphology of the UME tips before and after the measurements.

With continuing progress in probes and modes, as well as development of new cell designs and experimental setups, the SPM family of techniques can play a significant role in enhancing understanding of current and future LIB/SIB systems as well as other “beyond Li systems”. We provide the following perspectives for future directions in the use of SPM for battery materials.

- Samples more representative of (or taken from) realistic battery systems should be utilized for SPM study. While HOPG is highly desirable for SPM users because of how easy it is to obtain a nearly atomically flat scan area, its properties may be difficult to extrapolate to the graphite particles used in real LIBs. Similarly, single-crystal cathode substrates can be highly useful as a model system for fundamental study but only bear so much resemblance to a commercial battery electrode with its blend of conductive carbon, polymer binder, and polycrystalline active material. In fact, the carbon/binder matrix and its influence on the evolution of the active material properties is a relatively understudied area that requires more attention in order to fully understand the degradation of real rechargeable battery systems. In the future, automated SPM could be used for quality assurance and failure analysis on commercial lithium-ion battery materials, similar to the current usage of automated AFM in semiconductor facilities.
- Further innovations in EC-AFM cells are needed to better align the counter and working electrodes and improve ion conduction around the probe to ensure the reported current density reflects what is under the probe. Current cell designs may offset the electrodes’ position or have the counter electrode smaller than the working electrode, making it difficult for electrochemical processes to proceed ideally. These innovations may come in the form of a closed cell with the counter electrode placed adjacent to the probe tip or a counter electrode placed on or near the probe holder.
- Continued efforts to colocalize SPM techniques with chemical characterization techniques such as TEM/energy-dispersive X-ray spectroscopy (EDS), TOF-SIMS, and TERS/SERS are needed. This is especially true for the study of SEI; the mechanical and electrical data that can be obtained with SPM is useful but is only part of the full picture of the relation between the electrolyte composition, formation protocol, chemical composition, and properties that underlies the SEI.

Data from techniques such as XPS and standard Raman spectroscopy is collected over a larger area than typically sampled by SPM, which can aid this understanding but cannot ultimately provide information correlating to the property heterogeneity accessible by SPM. Note that some chemical characterization techniques are destructive, therefore must occur after the non-destructive or less destructive SPM techniques.

- Enhancements in image resolution and acquisition time are welcome for any characterization technique, but improved high-speed AFM could greatly increase the versatility of *operando* experiments, increasing temporal resolution and the granularity of data. As mentioned previously, reactions that occur faster than the data collection rate of SPM are only partially characterized. Currently, it takes several minutes to capture a frame of useful size and resolution. Tip velocity, pixel resolution, and aspect ratio can be manipulated to reduce acquisition time (and therefore increase temporal resolution), but come with corresponding losses in image size or detail, making representative data that can be accurately measured hard to obtain. Implementation of *operando* high-speed AFM could allow greater understanding of morphological and mechanical changes during SEI formation, alkali metal deposition and stripping, and cycling of intercalation electrodes.

We believe that with great care given to the experimental conditions and nature of samples as well as further development of advanced SPM modes and integration with other characterization techniques, SPM can continue to unveil exciting new discoveries in rechargeable alkali-ion batteries and guide future design of materials for beyond Li-ion batteries.

ACKNOWLEDGEMENTS

JAR and HX acknowledge the support by the U.S. Department of Energy, Office of Science, Office of Basic Energy Sciences program under Award Number DE-SC0019121. PHD and CME are supported in part by the National Institutes of Health under the Institutional Development Awards Program of the National Institute of General Medical Sciences via grant #P20GM148321.

REFERENCES

1 Y. Ding, Z. P. Cano, A. Yu, J. Lu and Z. Chen, *Electrochem. Energy Rev.*, 2019, **2**, 1–28.
2 J.-M. Tarascon and M. Armand, *Nature*, 2001, **414**, 359–367.
3 B. Voigtländer, *Atomic Force Microscopy*, Springer International Publishing, Cham, 2019.
4 G. Binnig, H. Rohrer, Ch. Gerber and E. Weibel, *Phys. Rev. Lett.*, 1982, **49**, 57–61.
5 M. Armand and J.-M. Tarascon, *Nature*, 2008, **451**, 652–657.
6 K. Xu, *Electrolytes, Interfaces and Interphases: Fundamentals and Applications in Batteries*, Royal Society of Chemistry, 12.
7 Y. S. Meng, V. Srinivasan and K. Xu, *Science*, 2022, **378**, eabq3750.
8 J. B. Goodenough and Y. Kim, *Chem. Mater.*, 2010, **22**, 587–603.
9 K. Xu, *Chem. Rev.*, 2004, **104**, 4303–4418.
10 M. Winter, *Z. Für Phys. Chem.*, 2009, **223**, 1395–1406.
11 A. v. Cresce, S. M. Russell, D. R. Baker, K. J. Gaskell and K. Xu, *Nano Lett.*, 2014, **14**, 1405–1412.
12 S. Wang, K. Yang, F. Gao, D. Wang and C. Shen, *RSC Adv.*, 2016, **6**, 77105–77110.
13 J. Zhang, R. Wang, X. Yang, W. Lu, X. Wu, X. Wang, H. Li and L. Chen, *Nano Lett.*, 2012, **12**, 2153–2157.

14 N.-W. Li, Y. Shi, Y.-X. Yin, X.-X. Zeng, J.-Y. Li, C.-J. Li, L.-J. Wan, R. Wen and Y.-G. Guo, *Angew. Chem. Int. Ed.*, 2018, **57**, 1505–1509.
15 J. Zheng, H. Zheng, R. Wang, L. Ben, W. Lu, L. Chen, L. Chen and H. Li, *Phys. Chem. Chem. Phys.*, 2014, **16**, 13229–13238.
16 H. Shin, W. Lu and J. Park, *ECS Meet. Abstr.*, 2016, **MA2016-03**, 604.
17 H. Shin, J. Park, S. Han, A. M. Sastry and W. Lu, *J. Power Sources*, 2015, **277**, 169–179.
18 Y. Wang, S. Song, C. Xu, N. Hu, J. Molenda and L. Lu, *Nano Mater. Sci.*, 2019, **1**, 91–100.
19 M. Dirican, C. Yan, P. Zhu and X. Zhang, *Mater. Sci. Eng. R Rep.*, 2019, **136**, 27–46.
20 K. M. Abraham, *ACS Energy Lett.*, 2020, **5**, 3544–3547.
21 N. Yabuuchi, K. Kubota, M. Dahbi and S. Komaba, *Chem. Rev.*, 2014, **114**, 11636–11682.
22 C. Delmas, *Adv. Energy Mater.*, 2018, **8**, 1703137.
23 A. Eftekhari, *ACS Sustain. Chem. Eng.*, 2019, **7**, 3684–3687.
24 C. Delmas, *Adv. Energy Mater.*, 2018, **8**, 1703137.
25 P. K. Nayak, L. Yang, W. Brehm and P. Adelhelm, *Angew. Chem. Int. Ed.*, 2018, **57**, 102–120.
26 W.-J. Zhang, *J. Power Sources*, 2011, **196**, 13–24.
27 H. Zhang, Y. Yang, D. Ren, L. Wang and X. He, *Energy Storage Mater.*, 2021, **36**, 147–170.
28 L. A. Selis and J. M. Seminario, *RSC Adv.*, 2018, **8**, 5255–5267.
29 S. Wang, X. Yin, D. Liu, Y. Liu, X. Qin, W. Wang, R. Zhao, X. Zeng and B. Li, *J. Mater. Chem. A*, 2020, **8**, 18348–18357.
30 M. Kitta and H. Sano, *Langmuir*, 2017, **33**, 1861–1866.
31 D. Stępień, B. Wolff, T. Diemant, G.-T. Kim, F. Hausen, D. Bresser and S. Passerini, *ACS Appl. Mater. Interfaces*, 2023, **15**, 25462–25472.
32 I. Yoon, S. Jurng, D. P. Abraham, B. L. Lucht and P. R. Guduru, *Energy Storage Mater.*, 2020, **25**, 296–304.
33 G. Binnig, C. F. Quate and Ch. Gerber, *Phys. Rev. Lett.*, 1986, **56**, 930–933.
34 S. An, *Appl. Sci. Converg. Technol.*, 2022, **31**, 99–102.
35 K. Xu, W. Sun, Y. Shao, F. Wei, X. Zhang, W. Wang and P. Li, *Nanotechnol. Rev.*, 2018, **7**, 605–621.
36 Q. P. McAllister, K. E. Strawhecker, C. R. Becker and C. A. Lundgren, *J. Power Sources*, 2014, **257**, 380–387.
37 H.-J. Butt, B. Cappella and M. Kappl, *Surf. Sci. Rep.*, 2005, **59**, 1–152.
38 K. A. Hirasawa, T. Sato, H. Asahina, S. Yamaguchi and S. Mori, *J. Electrochem. Soc.*, 1997, **144**, L81–L84.
39 A. C. Chu, J. Y. Josefowicz and G. C. Farrington, *J. Electrochem. Soc.*, 1997, **144**, 4161–4169.
40 Z. Zhang, S. Said, K. Smith, R. Jervis, C. A. Howard, P. R. Shearing, D. J. L. Brett and T. S. Miller, *Adv. Energy Mater.*, 2021, 2101518.
41 S. D. Lacey, J. Wan, A. von W. Cresce, S. M. Russell, J. Dai, W. Bao, K. Xu and L. Hu, *Nano Lett.*, 2015, **15**, 1018–1024.
42 L. Martin, H. Martinez, D. Poinot, B. Pecquenard and F. Le Cras, *J. Power Sources*, 2014, **248**, 861–873.
43 M. Han, C. Zhu, Q. Zhao, C. Chen, Z. Tao, W. Xie, F. Cheng and J. Chen, *ACS Appl. Mater. Interfaces*, 2017, **9**, 28620–28626.
44 W. Lu, J. Zhang, J. Xu, X. Wu and L. Chen, *ACS Appl. Mater. Interfaces*, 2017, **9**, 19313–19318.
45 C. Shen, G. Hu, L. Cheong, S. Huang, J. Zhang and D. Wang, *Small Methods*, 2018, **2**, 1700298.
46 C. Li, S. Minne, B. Pittenger and A. Mednick, *Simultaneous Electrical and Mechanical Property Mapping at the Nanoscale with PeakForce TUNA*, Bruker Corporation, 2011.
47 S. Yu. Luchkin, S. A. Lipovskikh, N. S. Katorova, A. A. Savina, A. M. Abakumov and K. J. Stevenson, *Sci. Rep.*, 2020, **10**, 8550.

48 M. G. Verde, L. Baggetto, N. Balke, G. M. Veith, J. K. Seo, Z. Wang and Y. S. Meng, *ACS Nano*, 2016, **10**, 4312–4321.
49 M. Otoyama, T. Yamaoka, H. Ito, Y. Inagi, A. Sakuda, M. Tatsumisago and A. Hayashi, *J. Phys. Chem. C*, 2021, **125**, 2841–2849.
50 X. Zhu, C. S. Ong, X. Xu, B. Hu, J. Shang, H. Yang, S. Katlakunta, Y. Liu, X. Chen, L. Pan, J. Ding and R.-W. Li, *Sci. Rep.*, 2013, **3**, 1084.
51 W. Yao, F. Long and R. Shahbazian-Yassar, *ACS Appl. Mater. Interfaces*, 2016, **8**, 29391–29399.
52 J. Zhu, L. Lu and K. Zeng, *ACS Nano*, 2013, **7**, 1666–1675.
53 M. Nonnenmacher, M. P. O'Boyle and H. K. Wickramasinghe, *Appl. Phys. Lett.*, 1991, **58**, 2921–2923.
54 J. M. R. Weaver and D. W. Abraham, *J. Vac. Sci. Technol. B Microelectron. Nanometer Struct. Process. Meas. Phenom.*, 1991, **9**, 1559–1561.
55 C. M. Efaw, T. da Silva, P. H. Davis, L. Li, E. Graugnard and M. F. Hurley, *J. Electrochem. Soc.*, 2019, **166**, C3018.
56 X. Zhu, R. I. Revilla and A. Hubin, *J. Phys. Chem. C*, 2018, **122**, 28556–28563.
57 J. Wu, S. Yang, W. Cai, Z. Bi, G. Shang and J. Yao, *Sci. Rep.*, 2017, **7**, 11164.
58 S. Choi, W. Toaran, S. H. Kim, Y. J. Song and Y.-J. Kim, *J. Alloys Compd.*, 2023, **943**, 169029.
59 H. Masuda, K. Matsushita, D. Ito, D. Fujita and N. Ishida, *Commun. Chem.*, 2019, **2**, 140.
60 C. Örnek, M. Liu, J. Pan, Y. Jin and C. Leygraf, *Top. Catal.*, 2018, **61**, 1169–1182.
61 T. Muster and A. E. Hughes, *J. Electrochem. Soc.*, 2006, **153**, B474–B485.
62 M. F. Hurley, C. M. Efaw, P. H. Davis, J. R. Croteau, E. Graugnard and N. Birbilis, *CORROSION*, 2015, **71**, 160–170.
63 A. J. Bard, F. R. F. Fan, Juhyoun. Kwak and Ovadia. Lev, *Anal. Chem.*, 1989, **61**, 132–138.
64 A. J. Bard and L. R. Faulkner, *Electrochemical Methods: Fundamentals and Applications*, Wiley, 2nd edn., 2000.
65 H. Xiong, University of Pittsburgh, 2007.
66 M. Carano and A. M. Bond, *Aust. J. Chem.*, 2007, **60**, 29.
67 H. Bülter, F. Peters, J. Schwenzel and G. Wittstock, *Angew. Chem. Int. Ed.*, 2014, **53**, 10531–10535.
68 C. D. Quilty, G. P. Wheeler, L. Wang, A. H. McCarthy, S. Yan, K. R. Tallman, M. R. Dunkin, X. Tong, S. Ehrlich, L. Ma, K. J. Takeuchi, E. S. Takeuchi, D. C. Bock and A. C. Marschilok, *Acs Appl. Mater. Interfaces*, 2021, **13**, 50920–50935.
69 Z. T. Gossage, J. Hui, Y. Zeng, H. Flores-Zuleta and J. Rodríguez-López, *Chem. Sci.*, 2019, **10**, 10749–10754.
70 G. A. Snook, T. D. Huynh, A. F. Hollenkamp and A. S. Best, *J. Electroanal. Chem.*, 2012, **687**, 30–34.
71 F. Xu, B. Baek and C. Jung, *J. Solid State Electrochem. - J SOLID STATE ELECTROCHEM*, DOI:10.1007/s10008-011-1325-8.
72 D. Huang, C. Engtrakul, S. Nanayakkara, D. W. Mulder, S.-D. Han, M. Zhou, H. Luo and R. C. Tenent, *ACS Appl. Mater. Interfaces*, 2021, **13**, 11930–11939.
73 D. Huang, C. Engtrakul, S. U. Nanayakkara, H. Luo and R. Tenent, *ECS Meet. Abstr.*, 2020, **MA2020-02**, 159.
74 A. J. Bard and M. V. Mirkin, Eds., *Scanning electrochemical microscopy*, CRC Press, Boca Raton London New York, Third edition., 2022.
75 D. Polcari, P. Dauphin-Ducharme and J. Mauzeroll, *Chem. Rev.*, 2016, **116**, 13234–13278.
76 A. Mishra, D. Sarbapalli, O. Rodríguez and J. Rodríguez-López, *Annu. Rev. Anal. Chem.*, 2023, **16**, 93–115.
77 A. Preet and T.-E. Lin, *Catalysts*, 2021, **11**, 594.
78 N. Ebejer, M. Schnippering, A. W. Colburn, M. A. Edwards and P. R. Unwin, *Anal. Chem.*, 2010, **82**, 9141–9145.

79 M. E. Snowden, M. Dayeh, N. A. Payne, S. Gervais, J. Mauzeroll and S. B. Schougaard, *J. Power Sources*, 2016, **325**, 682–689.
80 B. Tao, L. C. Yule, E. Daviddi, C. L. Bentley and P. R. Unwin, *Angew. Chem. Int. Ed.*, 2019, **58**, 4606–4611.
81 D. Martin-Yerga, M. Kang and P. R. Unwin, *Chemelectrochem*, 2021, **8**, 4240–4251.
82 C. G. Williams, M. A. Edwards, A. L. Colley, J. V. Macpherson and P. R. Unwin, *Anal. Chem.*, 2009, **81**, 2486–2495.
83 G. Jayamaha, M. Maleki, C. L. Bentley and M. Kang, *The Analyst*, 2024, 10.1039.D4AN00117F.
84 O. J. Wahab, M. Kang and P. R. Unwin, *Curr. Opin. Electrochem.*, 2020, **22**, 120–128.
85 N. Ebejer, A. G. Güell, S. C. S. Lai, K. McKelvey, M. E. Snowden and P. R. Unwin, *Annu. Rev. Anal. Chem. Palo Alto Calif*, 2013, **6**, 329–351.
86 E. Peled, D. Golodnitsky and G. Ardel, *J. Electrochem. Soc.*, 1997, **144**, L208–L210.
87 D. Aurbach, B. Markovsky, M. D. Levi, E. Levi, A. Schechter, M. Moshkovich and Y. Cohen, *J. Power Sources*, 1999, **81–82**, 95–111.
88 H. Wu, H. Jia, C. Wang, J.-G. Zhang and W. Xu, *Adv. Energy Mater.*, 2021, **11**, 2003092.
89 Y. Chu, Y. Shen, F. Guo, X. Zhao, Q. Dong, Q. Zhang, W. Li, H. Chen, Z. Luo and L. Chen, *Electrochem. Energy Rev.*, 2020, **3**, 187–219.
90 B. Horstmann, F. Single and A. Latz, *Curr. Opin. Electrochem.*, 2019, **13**, 61–69.
91 Z. Wang, H. Yang, Y. Liu, Y. Bai, G. Chen, Y. Li, X. Wang, H. Xu, C. Wu and J. Lu, *Small*, 2020, **16**, 2003268.
92 W.-W. Wang, Y. Gu, H. Yan, S. Li, J.-W. He, H.-Y. Xu, Q.-H. Wu, J.-W. Yan and B.-W. Mao, *Chem*, 2020, **6**, 2728–2745.
93 Y. Chen, W. Wu, S. Gonzalez-Munoz, L. Forcieri, C. Wells, S. P. Jarvis, F. Wu, R. Young, A. Dey, M. Isaacs, M. Nagarathinam, R. G. Palgrave, N. Tapia-Ruiz and O. V. Kolosov, *Nat. Commun.*, 2023, **14**, 1321.
94 Y. Gao, X. Du, Z. Hou, X. Shen, Y.-W. Mai, J.-M. Tarascon and B. Zhang, *Joule*, 2021, **5**, 1860–1872.
95 S. Yuan, S. Weng, F. Wang, X. Dong, Y. Wang, Z. Wang, C. Shen, J. L. Bao, X. Wang and Y. Xia, *Nano Energy*, 2021, **83**, 105847.
96 X. Zhang, J. Yang, Z. Ren, K. Xie, Q. Ye, F. Xu and X. Liu, *New Carbon Mater.*, 2022, **37**, 371–379.
97 C. Wang, A. C. Thenuwara, J. Luo, P. P. Shetty, M. T. McDowell, H. Zhu, S. Posada-Pérez, H. Xiong, G. Hautier and W. Li, *Nat. Commun.*, 2022, **13**, 4934.
98 S. Li, C. Wang, C. Meng, Y. Ning, G. Zhang and Q. Fu, *J. Energy Chem.*, 2022, **67**, 718–726.
99 H. Zhang, D. Wang and C. Shen, *Appl. Surf. Sci.*, 2020, **507**, 145059.
100 S. Daboss, T. Philipp, K. Palanisamy, J. Flowers, H. S. Stein and C. Kranz, *Electrochimica Acta*, 2023, **453**, 142345.
101 R. Zhao, S. Wang, D. Liu, Y. Liu, X. Lv, X. Zeng and B. Li, *ACS Appl. Energy Mater.*, 2021, **4**, 492–499.
102 Z. Zhang, K. Smith, R. Jervis, P. R. Shearing, T. S. Miller and D. J. L. Brett, *ACS Appl. Mater. Interfaces*, 2020, **12**, 35132–35141.
103 L. Tao, J. A. Russell, D. Xia, B. Ma, S. Hwang, Z. Yang, A. Hu, Y. Zhang, P. Sittisomwong, D. Yu, P. A. Deck, L. A. Madsen, H. Huang, H. Xiong, P. Bai, K. Xu and F. Lin, *J. Am. Chem. Soc.*, 2023, **145**, 16538–16547.
104 L. A. Ma, A. J. Naylor, L. Nyholm and R. Younesi, *Angew. Chem. Int. Ed.*, 2021, **60**, 4855–4863.
105 R. Mogensen, D. Brandell and R. Younesi, *ACS Energy Lett.*, 2016, **1**, 1173–1178.
106 M. Fei, L. Qi, S. Han, Y. Li, H. Xi, Z. Lin, J. Wang, C. Ducati, M. Chhowalla, R. V. Kumar, Y. Jin and J. Zhu, *Angew. Chem. Int. Ed.*, 2024, **63**, e202409719.
107 H. Zhu, J. A. Russell, Z. Fang, P. Barnes, L. Li, CoreyM. Efaw, A. Muenzer, J. May, K. Hamal, I. F. Cheng, P. H. Davis, EricJ. Dufek and H. Xiong, *Small*, 2021, **17**, 2105292.
108 Y. Shi, G.-X. Liu, J. Wan, R. Wen and L.-J. Wan, *Sci. China Chem.*, 2021, **64**, 734–738.

109 C. Stetson, Y. Yin, A. Norman, S. P. Harvey, M. Schnabel, C. Ban, C.-S. Jiang, S. C. DeCaluwe and M. Al-Jassim, *J. Power Sources*, 2021, **482**, 228946.
110 X. Xu, D. Martín-Yerga, N. E. Grant, G. West, S. L. Pain, M. Kang, M. Walker, J. D. Murphy and P. R. Unwin, *Small*, 2023, 2303442.
111 D. Martín-Yerga, D. C. Milan, X. Xu, J. Fernández-Vidal, L. Whalley, A. J. Cowan, L. J. Hardwick and P. R. Unwin, *Angew. Chem. Int. Ed.*, 2022, **61**, e202207184.
112 C. S. Santos, A. Botz, A. S. Bandarenka, E. Ventosa and W. Schuhmann, *Angew. Chem. Int. Ed.*, 2022, **61**, e202202744.
113 S. Said, Z. Zhang, R. R. C. Shutt, H. J. Lancaster, D. J. L. Brett, C. A. Howard and T. S. Miller, *ACS Nano*, 2023, **17**, 6220–6233.
114 J. D. McBrayer, C. A. Apblett, K. L. Harrison, K. R. Fenton and S. D. Minteer, *Nanotechnology*, 2021, **32**, 502005.
115 C. Monroe and J. Newman, *J. Electrochem. Soc.*, 2005, **152**, A396.
116 J.-X. Tian, H.-J. Guo, J. Wan, G.-X. Liu, R. Wen and L.-J. Wan, *Sci. China Chem.*, 2023, **66**, 2921–2928.
117 H.-J. Guo, Y. Sun, Y. Zhao, G.-X. Liu, Y.-X. Song, J. Wan, K.-C. Jiang, Y.-G. Guo, X. Sun and R. Wen, *Angew. Chem. Int. Ed.*, 2022, **61**, e202211626.
118 M. Chen, W. Wang, Z. Shi, Z. Liu and C. Shen, *Appl. Surf. Sci.*, 2022, **600**, 154119.
119 K. Xu, *Chem. Rev.*, 2014, **114**, 11503–11618.
120 S. Wang, D. Liu, X. Cai, L. Zhang, Y. Liu, X. Qin, R. Zhao, X. Zeng, C. Han, C. Zhan, F. Kang and B. Li, *Nano Energy*, 2021, **90**, 106510.
121 Q. Liu, L. Zhang, H. Sun, L. Geng, Y. Li, Y. Tang, P. Jia, Z. Wang, Q. Dai, T. Shen, Y. Tang, T. Zhu and J. Huang, *ACS Energy Lett.*, 2020, **5**, 2546–2559.
122 J. Holoubek, H. Liu, Z. Wu, Y. Yin, X. Xing, G. Cai, S. Yu, H. Zhou, T. A. Pascal, Z. Chen and P. Liu, *Nat. Energy*, 2021, **6**, 303–313.
123 X. Zhou, Q. Zhang, Z. Zhu, Y. Cai, H. Li and F. Li, *Angew. Chem. Int. Ed.*, 2022, anie.202205045.
124 S. Chen, J. Zheng, D. Mei, K. S. Han, M. H. Engelhard, W. Zhao, W. Xu, J. Liu and J. Zhang, *Adv. Mater.*, 2018, **30**, 1706102.
125 X. Ren, S. Chen, H. Lee, D. Mei, M. H. Engelhard, S. D. Burton, W. Zhao, J. Zheng, Q. Li, M. S. Ding, M. Schroeder, J. Alvarado, K. Xu, Y. S. Meng, J. Liu, J.-G. Zhang and W. Xu, *Chem*, 2018, **4**, 1877–1892.
126 J. Ming, Z. Cao, W. Wahyudi, M. Li, P. Kumar, Y. Wu, J.-Y. Hwang, M. N. Hedhili, L. Cavallo, Y.-K. Sun and L.-J. Li, *ACS Energy Lett.*, 2018, **3**, 335–340.
127 H. Cheng, Q. Sun, L. Li, Y. Zou, Y. Wang, T. Cai, F. Zhao, G. Liu, Z. Ma, W. Wahyudi, Q. Li and J. Ming, *ACS Energy Lett.*, 2022, **7**, 490–513.
128 D. A. Rakov, F. Chen, S. A. Ferdousi, H. Li, T. Pathirana, A. N. Simonov, P. C. Howlett, R. Atkin and M. Forsyth, *Nat. Mater.*, 2020, **19**, 1096–1101.
129 L. K. S. Bonagiri, K. S. Panse, S. Zhou, H. Wu, N. R. Aluru and Y. Zhang, *ACS Nano*, 2022, **16**, 19594–19604.
130 K. S. Panse, H. Wu, S. Zhou, F. Zhao, N. R. Aluru and Y. Zhang, *J. Phys. Chem. Lett.*, 2022, **13**, 9464–9472.
131 S. Zhou, K. S. Panse, M. H. Motevaselian, N. R. Aluru and Y. Zhang, *ACS Nano*, 2020, **14**, 17515–17523.
132 T. Fukuma, Y. Ueda, S. Yoshioka and H. Asakawa, *Phys. Rev. Lett.*, 2010, **104**, 016101.
133 Y. Bao, M. Kitta, T. Ichii, T. Utsunomiya and H. Sugimura, *Jpn. J. Appl. Phys.*, 2021, **60**, SE1004.
134 Y. Yamagishi, H. Kominami, K. Kobayashi, Y. Nomura, E. Igaki and H. Yamada, *Nano Lett.*, 2022, **22**, 9907–9913.
135 A. Mishra, D. Sarbapalli, Md. S. Hossain, Z. T. Gossage, Z. Li, A. Urban and J. Rodríguez-López, *J. Electrochem. Soc.*, 2022, **169**, 086501.

136 A. Mishra, J.-W. Lin, B. Zahiri, P. V. Braun and J. Rodríguez-López, *J. Electrochem. Soc.*, 2024, **171**, 056510.
137 Y. Bi, J. Tao, Y. Wu, L. Li, Y. Xu, E. Hu, B. Wu, J. Hu, C. Wang, J.-G. Zhang, Y. Qi and J. Xiao, *Science*, 2020, **370**, 1313–1317.
138 J. S. Terreblanche, D. L. Thompson, I. M. Aldous, J. Hartley, A. P. Abbott and K. S. Ryder, *J. Phys. Chem. C*, 2020, **124**, 14622–14631.
139 R. S. Negi, S. P. Culver, M. Wiche, S. Ahmed, K. Volz and M. T. Elm, *Phys. Chem. Chem. Phys.*, 2021, **23**, 6725–6737.
140 K. Xu, *J. Power Sources*, 2023, **559**, 232652.
141 C. Shen, Y. Huang, J. Yang, M. Chen and Z. Liu, *Energy Storage Mater.*, 2021, **39**, 271–277.
142 C.-S. Jiang, Y. Yin, H. Guthrey, K. Park, S.-H. Lee and M. M. Al-Jassim, *J. Power Sources*, 2021, **481**, 229138.
143 E. J. Fuller, E. Strelcov, J. L. Weaver, M. W. Swift, J. D. Sugar, A. Kolmakov, N. Zhitenev, J. J. McClelland, Y. Qi, J. A. Dura and A. A. Talin, *ACS Energy Lett.*, 2021, **6**, 3944–3951.
144 N. Nioradze, R. Chen, J. Kim, M. Shen, P. Santhosh and S. Amemiya, *Anal. Chem.*, 2013, **85**, 6198–6202.

No primary research results, software or code have been included and no new data were generated or analysed as part of this perspective.